1 **Loss of Ena/VASP interferes with lamellipodium architecture, motility and integrin-**

2 **dependent adhesion**

3

4 Julia Damiano-Guercio[1], Laëtitia Kurzawa[2,*], Jan Mueller[3,*], Georgi Dimchev[4,*], Maria

5 Nemethova[3,*], Thomas Pokrant[1], Stefan Bruehmann[1], Joern Linkner[1], Laurent Blanchoin[2],

6 Michael Sixt[3], Klemens Rottner[4,5] and Jan Faix[1]

7

8 [1]Institute for Biophysical Chemistry, Hannover Medical School, Carl-Neuberg-Str. 1, 30625

9 Hannover, Germany; [2]CytoMorphoLab, UMR5168, Integrative Structural and Cellular

10 Biology Department, Interdisciplinary Research Institute of Grenoble, CEA, CNRS, INRA,

11 Grenoble-Alpes Univ., 17 rue des Martyrs, 38054, Grenoble, France. [3]Institute of Science and

12 Technology Austria (IST Austria), am Campus 1, 3400 Klosterneuburg, Austria; [4]Division of

13 Molecular Cell Biology, Zoological Institute, Technical University Braunschweig,

14 Spielmannstrasse 7, 38106 Braunschweig, Germany. [5]Molecular Cell Biology Group,

15 Helmholtz Centre for Infection Research, Inhoffenstrasse 7, 38124 Braunschweig, Germany.

16

17

18 *These authors contributed equally to this work.

19

20

21 Send correspondences to:

22 Jan Faix

23 Phone: +49-511-532-2928

24 Fax: +49-511-532-5966

25 Email: faix.jan@mh-hannover.de

26   **Abstract**

27   Cell migration entails networks and bundles of actin filaments termed lamellipodia and

28   microspikes or filopodia, respectively, as well as focal adhesions, all of which recruit

29   Ena/VASP family members hitherto thought to antagonize efficient cell motility. However,

30   we find these proteins to act as positive regulators of migration in different cell lines.

31   CRISPR/Cas9-mediated loss of Ena/VASP proteins reduced lamellipodial actin assembly and

32   perturbed lamellipodial architecture, as evidenced by changed network geometry as well as

33   reduction of filament length and number that was accompanied by abnormal Arp2/3 complex

34   and heterodimeric capping protein accumulation. Loss of Ena/VASP function also abolished

35   the formation of microspikes normally embedded in lamellipodia, but not of filopodia

36   capable of emanating without lamellipodia. Ena/VASP-deficiency also impaired integrin-

37   mediated adhesion accompanied by reduced traction forces exerted through these structures.

38   Our data thus uncover novel, cellular Ena/VASP functions of these actin polymerases that are

39   fully consistent with their promotion of cell migration.

40

41   **Introduction**

42   Adhesion and migration are invariably driven by continuous and dynamic actin cytoskeleton

43   remodeling (Blanchoin et al., 2014). The major protrusive structure of migrating cells on flat

44   and rigid substrata is the sheet-like lamellipodium (Letort et al., 2015; Rottner et al., 2017).

45   The extension of dense and branched actin filaments in the lamellipodium drives its growth

46   and pushes the membrane forward (Koestler et al., 2008; Mullins et al., 1998; Pollard and

47   Borisy, 2003; Vinzenz et al., 2012). Branching by Actin-related protein (Arp) 2/3 complex is

48   activated by the WAVE regulatory complex (WRC) downstream of Rac subfamily GTPase

49   signaling (Eden et al., 2002; Ismail et al., 2009; Molinie and Gautreau, 2018). Consistently,

50   knockdown or knockout of essential Arp2/3 complex (Suraneni et al., 2012; Wu et al., 2012)

2

51   or WRC subunits (Innocenti et al., 2004; Schaks et al., 2018; Steffen et al., 2004) or Rac

52   GTPases (Schaks et al., 2018; Steffen et al., 2013) all abrogated lamellipodium formation.

53   The lateral flow of actin filaments and bundles embedded in the lamellipodium, called

54   microspikes, is driven by actin assembly at the membrane (Oldenbourg et al., 2000). When

55   microspikes transform and protrude beyond the lamellipodium edge, they are called filopodia

56   (Small, 1988; Svitkina et al., 2003). Yet, in spite of both being built of parallel actin filament

57   bundles and sharing constituents, filopodia and microspikes display important differences. As

58   opposed to microspikes as integral parts of lamellipodial networks, filopodia can kink and

59   bend (Nemethova et al., 2008), arising independently and even in excess in the absence of

60   lamellipodia (Gupton et al., 2005; Koestler et al., 2013; Steffen et al., 2006; Wu et al., 2012).

61   Consistently, filopodia can form around the entire cell periphery and at the dorsal surface

62   (Block et al., 2008; Bohil et al., 2006; Pellegrin and Mellor, 2005). Moreover, rates of actin

63   polymerization in microspikes and lamellipodia are indistinguishable from each other (Lai et

64   al., 2008; Oldenbourg et al., 2000), whereas those in filopodia appear to be regulated

65   independently.

66   Filament elongation is driven by formins and Ena/VASP proteins. Formins are dimeric multi

67   domain proteins that remain tightly associated with growing filament barbed ends while

68   accelerating their growth (Kovar et al., 2006). Several formins such as mDia2 (Block et al.,

69   2008; Yang et al., 2007) and the formin-like family members 2 (FMNL2) and 3 (Block et al.,

70   2012; Harris et al., 2010; Kage et al., 2017; Young et al., 2018) localize at lamellipodia and

71   filopodia tips, and have been implicated in driving these protrusions and cell migration.

72   Ena/VASP family proteins localize to sites of active actin assembly including focal adhesions

73   (FA) (Gertler et al., 1996; Reinhard et al., 1995), stress fibers (Gateva et al., 2014; Rottner et

74   al., 2001), and lamellipodial or filopodial tips (Rottner et al., 1999; Svitkina et al., 2003).

75   Vertebrates harbor Vasodilator-stimulated phosphoprotein (VASP), mammalian Enabled

3

76   (Mena), and Ena-VASP-like (Evl). All family members are tetramers encompassing domains

77   allowing for interactions with FPPPP-containing proteins, actin monomers, profilin-actin

78   complexes and actin filaments (Bear and Gertler, 2009). Ena/VASP tetramers are poorly

79   processive, but processivity and resistance against heterodimeric capping protein that stops

80   barbed end growth, increases markedly upon oligomerization or clustering (Breitsprecher et

81   al., 2011a, 2008; Brühmann et al., 2017; Hansen and Mullins, 2015).

82   Genetic removal of all three Ena/VASP proteins was previously shown to abrogate filopodia

83   formation in neuronal cells (Kwiatkowski et al., 2007). The functions of Ena/VASP proteins

84   in cell motility have remained more controversial. Although VASP accumulation at

85   lamellipodia tips positively correlates with protrusion rates (Rottner et al., 1999), genetic

86   inactivation of VASP and Mena or mitochondrial Ena/VASP sequestration in fibroblasts was

87   reported to increase cell migration (Bear et al., 2002, 2000). This phenotype was explained by

88   lamellipodia protruding more persistently after interference with Ena/VASP function, and

89   containing shorter and more branched filaments. Excess of Ena/VASP, in contrast, generated

90   lamellipodia with longer, less branched filaments, prone to lifting rearwards during

91   membrane ruffling, therefore driving migration less efficiently (Bear et al., 2002). Despite

92   this negative role in fibroblast motility, the proposed positive regulatory function of

93   Ena/VASP on lamellipodial filaments was consistent with their clear relevance in the motility

94   of *Listeria* harboring the Ena/VASP ligand ActA (Geese et al., 2002; Loisel et al., 1999;

95   Skoble et al., 2001). Whether the reported negative correlation of Ena/VASP activity with

96   migration can be generalized, has remained unanswered.

97   Finally, although Ena/VASP proteins are prominent FA components, their roles in cell

98   substrate adhesion and FA formation have also remained controversial. Both inhibitory

99   (Galler et al., 2006) and stimulatory roles (Gupton et al., 2012; Kang et al., 2010; Puleo et al.,

100   2019; Young and Higgs, 2018) on adhesion were reported, whereas one study did not detect

4

101   any effect in fibroblasts lacking Mena and VASP (Bear et al., 2000). To resolve these

102   discrepancies, we characterized cells disrupted for individual, two or all three Ena/VASP

103   family members in distinct types of parental cells, and explored the impact of their individual

104   and collective removal on formation of different protrusion types, migration efficiency and

105   adhesion.

106

107   **Results**

108   **Loss of Ena/VASP impairs cell migration in B16-F1 cells**

109   To evaluate the physiological function of Ena/VASP proteins in a rapidly migrating cell type,

110   we sequentially inactivated the three Ena/VASP paralogues Evl, VASP and Mena using

111   CRISPR/Cas9 technology in B16-F1 mouse melanoma cells. Respective protein loss in

112   independent clonal cell lines was confirmed by immunoblotting and verified by sequencing

113   of genomic target sites (***Figure 1A, Supplement 1***). Migration rates of B16-F1 wild-type and

114   two independent lines of each genotype were then analyzed on laminin by phase-contrast,

115   time-lapse microscopy. Interestingly, consecutive Ena/VASP member removal caused an

116   increasing phenotype in migration rate, ranging from a comparably modest reduction of 1.25

117   ± 0.37 µm/min and 1.19 ± 0.47 µm/min for single Evl KO mutants (E-KO) as compared to

118   control (1.44 ± 0.4 µm/min), to 0.62 ± 0.25 µm/min and 0.57 ± 0.27 µm/min in Evl and

119   VASP double-KOs (EV-KO), and 0.47 ± 0.19 µm/min and 0.43 ± 0.22 µm/min in triple-KOs

120   (EVM-KO) (***Figure 1B, Figure 1-video 1***). This was accompanied by a gradual increase in

121   directionality culminating in EVM-KO cells that were 46% more directional as compared to

122   wild-type B16-F1 (***Figure 1C***). Quantitative analyses of the turning angles revealed an

123   incrementally increased frequency at 0° from 10.2% in wild-type to 12.3% in single KO,

124   16.1% in double KO and 16.9% in triple KO cells, in support of the higher directionality in

125   mutant cells that coincided with their reduced motility (***Figure 1D***). Since independently

126　　generated Ena/VASP mutant cell lines behaved highly similar in distinct assays, data derived

127　　from one triple-KO clone (#23.7.66) are shown below. To ensure that observed phenotypes

128　　were Ena/VASP-specific, the same parameters were analyzed in reconstituted EVM-KO

129　　mutant cells ectopically expressing EGFP-tagged VASP, Evl or Mena. Re-expression of

130　　VASP, which was found to contribute most efficiently to motility, largely rescued cell speed,

131　　directionality and frequency of turning angles (***Figure 1E-F, Figure 1-figure supplement***

132　　***1A***). The rescue experiments with EGFP-tagged Evl or Mena yielded similar results, but

133　　these proteins were slightly less effective in restoring cell speed (***Figure 1E-F***). Finally, we

134　　calculated the mean square displacement (MSD) in wild-type and the entire collection of

135　　mutant cells to assess their effective directional movement. Despite their higher

136　　directionality, presumably owing to their considerably slower motility, all Ena/VASP mutant

137　　cells displayed incrementally decreasing and lower MSD values as compared to control

138　　(***Figure 1G***). Notably, in EVM-KO cells rescued with EGFP-tagged VASP, Evl or Mena, the

139　　MSD values were again markedly increased (***Figure 1-figure supplement 1B***).

140

141　　**Ena/VASP-deficiency consistently diminishes cell migration in fibroblasts**

142　　To corroborate our findings in strongly adherent cell types, we first examined MV^{D7} mouse

143　　embryonic fibroblasts. This cell line was described previously to derive from Mena/VASP-

144　　deficient mice and selected initially to lack detectable expression of Evl (Bear et al., 2000),

145　　albeit later stated to contain trace amounts (Auerbuch et al., 2003). We did confirm the

146　　absence of Mena and VASP in these cells by immunoblotting (***Figure 2A***). Surprisingly,

147　　however, our newly-generated antibodies raised against and affinity-purified with Evl (see

148　　Materials and Methods) now identified the protein at low, but clearly detectable levels in this

149　　cell line. Thus, to obtain fibroblasts devoid of all three Ena/VASP proteins, we employed

150　　CRISPR/Cas9 to eliminate Evl in MV^{D7} cells, with Evl disruption confirmed by

6

151   immunoblotting and sequencing as described for B16-F1 cells above (*Figure 2A,*

152   *Supplement 1*). Since distinct triple-KO cell lines behaved again in a highly comparable

153   fashion, only data from clone #31 referred to as MVE-KO are shown. We first analyzed

154   migration on fibronectin by phase-contrast time-lapse imaging of MV^{D7} and MVE-KO as

155   well as MVE-KO cells rescued with EGFP-tagged Evl. In MVE-KO, cell speed (0.41 ± 0.17

156   µm/min) was significantly reduced as compared to MV^{D7} control (0.56 ± 0.19 µm/min),

157   whereas migration of MVE-KO cells expressing EGFP-Evl (0.68 ± 0.28 µm/min) was

158   markedly increased (*Figure 2B*). Remarkably, in spite of their higher cell speed, MV^{D7}

159   exhibited even lower MSD values than MVE-KO cells (*Figure 2C*), apparently caused by the

160   lower directionality of the former, and as evidenced by their trajectories in radar plots

161   (*Figure 2-figure supplement 1A-B*). As expected, triple-KO cells reconstituted with Evl

162   displayed strongly increased MSD values (*Figure 2C*) and decreased directionality (*Figure*

163   *2-figure supplement 1A-B*).

164   Additionally, we analyzed directional cell migration of these cell lines in wound closure

165   scratch assays (*Figure 2D*). Average wound closure rates were reduced by 24% in MVE-KO

166   cells (18121 ± 2658 µm²h^{-1}) as compared to MV^{D7} cells (23906 ± 2042 µm²h^{-1}) (*Figure 2E*).

167   Interestingly, reconstitution of MVE-KO cells with stable Evl expression significantly

168   increased wound closure to rates virtually identical to MV^{D7} controls (*Figure 2F*). Thus,

169   despite comparably low expression of Evl in MV^{D7} fibroblasts, its elimination caused clearly

170   detectable impairment of cell migration.

171   To assess the contribution of the two other Ena/VASP family members in fibroblast motility,

172   we also disrupted the genes encoding Mena and VASP individually or in combination in

173   mouse NIH 3T3 fibroblasts by CRISPR/Cas9 technology, and again confirmed elimination of

174   respective proteins by immunoblotting and sequencing (*Figure 2G*, *Supplement 1*).

175   Migration rates of NIH 3T3 wild-type and two independent lines of each genotype were then

176   again analyzed on fibronectin by phase-contrast time-lapse imaging. Comparable to the

177   findings in B16-F1 cells, consecutive removal of Mena and VASP in NIH 3T3 cells also

178   caused a step-wise increase in migration phenotype, ranging from a rather modest average

179   reduction of about 10.6% for single Mena KO mutants (M-KO) to 31.6% in Mena and VASP

180   double-KO (MV-KO) mutants as compared to control (***Figure 2H***). Consistently, these

181   Ena/VASP mutant cells also exhibited incrementally decreasing and lower MSD values as

182   compared to NIH 3T3 wild-type controls (***Figure 2I***). All these findings combined, strongly

183   suggest, quite strikingly, that Ena/VASP proteins execute conserved and prominent, positive

184   regulatory functions in cell migration, in a fashion irrespective of cell type (melanoma cells

185   and fibroblast alike) and thus type of mesenchymal migration and/or signaling condition, as

186   induced by extracellular matrices (laminin *versus* fibronectin).

187   To relate the specific contributions of individual Ena/VASP family members to cell

188   migration, we finally determined the cellular concentrations of expressed orthologues in B16-

189   F1, NIH 3T3 and MV^{D7} cells. For this, we titrated defined amounts of recombinant proteins

190   with total cell lysates from a given number of cells in immunoblots, and calculated resulting

191   absolute levels of each protein in the different cell types (***Figure 2J***). Interestingly, in spite of

192   considerably higher expression of Mena in B16-F1 and NIH 3T3 cells as compared to VASP,

193   and in particular relative to Evl, loss of Mena affected migration much less strongly than, for

194   instance, removal of VASP. This suggests a certain differentiation of Ena/VASP family

195   member function despite clearly overlapping functions.

196

197   **Loss of Ena/VASP reduces lamellipodium width and abrogates microspike formation**

198   Since migration is mainly driven by actin assembly in the lamellipodium, we then analyzed

199   actin filament (F-actin) distribution in B16-F1 and EVM-KO cells after phalloidin staining.

200   As opposed to B16-F1 control cells, which displayed prominent lamellipodia with numerous

201   microspikes, EVM-KO cells developed strongly compromised lamellipodia largely lacking

202   microspikes (*Figure 3A, Figure 3-video 1*). Quantification of F-actin contents in

203   lamellipodia revealed about 45% reduction in the triple mutant, and the average width of

204   lamellipodia was diminished by about 65% to 0.8 ± 0.2 µm when compared to wild-type with

205   2.3 ± 0.7 µm. In mutant cells reconstituted with EGFP-VASP, F-actin intensity increased

206   even 40% above wild-type levels, and lamellipodium width was readily restored to 2.7 ± 0.8

207   µm (*Figure 3B-C*). Similar, but less pronounced effects were found after rescue with EGFP-

208   tagged Evl or Mena as compared to VASP (*Figure 3-figure supplement 1A-C*). Given the

209   evident lack of microspikes, we stained for the actin-crosslinking protein fascin, a well-

210   established constituent of microspikes in B16-F1 cells (Vignjevic et al., 2006). Again, the

211   triple mutant virtually lacked fascin-containing bundles, as opposed to wild-type and

212   reconstituted mutants expressing VASP, despite unchanged expression of fascin in the mutant

213   (*Figure 3D-G*). This was corroborated by imaging of wild-type and EVM-KO cells

214   expressing EGFP-fascin (**Figure 3-*video 2***). Finally, we examined the gene dose-dependent

215   requirement for Ena/VASP family members in microspike formation and found that virtually

216   complete loss of microspikes was observed only upon disruption of all three family members

217   (*Figure 3H*).

218

219   **Potent filopodia inducers fail to rescue microspike formation in Ena/VASP-deficient**

220   **cells**

221   We then asked whether microspikes can be reformed in the triple-mutant upon transient

222   expression of potent factors known to induce peripheral protrusions, and in particular related

223   protrusive structures such as filopodia (Block et al., 2008; Bohil et al., 2006; Kage et al.,

224   2017; Pellegrin and Mellor, 2005). We also used all Ena/VASP members as controls. Evl and

225   Mena both rescued canonical lamellipodia with microspikes in EVM-KO comparable to

9

226   VASP, with Mena forming microspikes above average length (***Figure 4A, Figure 4-figure***

227   ***supplement 1A-B***). Strikingly, none of the agents established previously to be capable of

228   inducing filopodia formation, i.e. constitutively active variants of the small Rho GTPase Rif

229   (L77), the formins mDia2 (mDia2ΔDAD), FMNL3 (E275) and to lesser extent FMNL2

230   (E272), or unconventional myosin X were able to restore microspike-containing lamellipodia,

231   indicating that microspike formation requires more specific activities that are critically

232   dependent on Ena/VASP function (***Figure 4A***).

233   To explore this potential molecular difference between microspikes and filopodia more

234   directly, we induced filopodia in the absence of lamellipodia in B16-F1 and EVM-KO cells.

235   Since it is commonly assumed that lamellipodia emerge by extension of Arp2/3 complex-

236   generated, dendritic filament networks downstream of WRC and Rac signaling (Pollard,

237   2007; Schaks et al., 2018; Steffen et al., 2013; Wu et al., 2012), we inhibited Arp2/3 complex

238   with high concentrations of CK666 in combination with cell seeding on low concentrations of

239   laminin, which aided inhibitor-mediated suppression of lamellipodia formation in these

240   conditions (data not shown). Analyses of phalloidin-stained cells revealed that albeit reduced

241   in formation frequency per cell, filopodia formation was still possible in EVM-KO cells (66%

242   compared to B16-F1 control on low laminin). This confirmed that Ena/VASP family can

243   indeed contribute to filopodia formation, as previously observed in *D. discoideum* (Han et al.,

244   2002). At the same time, these data also illustrated that filopodia can indeed form to

245   significant extent without lamellipodia, e.g. upon inhibition of Arp2/3 complex and thus in

246   the absence of microspikes (***Figure 4B-C***), in spite of the reduced frequencies of filopodia

247   formation observed here. Conversely, however, induction of filopodia formation by

248   expression of constitutive active mDia2 (Block et al., 2008; Yang et al., 2007) was virtually

249   identical in the EVM-KO mutant as compared to B16-F1 cells (***Figure 4D-E***), supporting the

250   view of multiple pathways leading to filopodium formation (Young et al., 2015).

251

Loss of Ena/VASP changes distribution of Arp2/3 complex and capping protein and affects lamellipodial dynamics

254 To explore if or how loss of Ena/VASP function affected Arp2/3 complex accumulation, we

255 immunolabelled the cells for the Arp2/3 complex and found that it accumulated in a

256 peripheral band much narrower than commonly observed in wild-type lamellipodia (reduced

257 by 64%), but with roughly 75% higher intensity at the tips of mutant lamellipodia (*Figure*

258 *5A-C*). The mutant phenotype was again Ena/VASP-specific, since it was perfectly rescued

259 by transient expression of EGFP-tagged VASP and Evl, and at least partly by Mena. More

260 specifically, VASP was slightly more effective than Evl, and Mena was capable of mediating

261 a statistically significant rescue only concerning width of observed Arp2/3 complex signal

262 (*Figure 5A-C*, *Figure 5-figure supplement 1A-C*). We also monitored the distributions of

263 heterodimeric capping protein (CP), the F-actin binding protein cortactin and the WRC-

264 subunit WAVE2. CP and cortactin distributions were highly reminiscent of changes in

265 Arp2/3, again much narrower (reduced by 60% and 67%, respectively), and with

266 approximately 75% and 60% increased intensities in EVM-KO as compared to controls

267 (*Figure 5D-F*, *Figure 5-figure supplement 1D-I*). Interestingly, we found no noticeable

268 difference in distribution and intensity of WAVE2 in wild-type *versus* EVM-KO (*Figure 5-*

269 *figure supplement 1J-L*). This together with reversion to or close to wild-type levels of

270 Arp2/3 complex, CP and cortactin by EGFP-tagged Ena/VASP family members illustrated

271 their impact on the lamellipodial Arp2/3 complex machinery downstream, and thus

272 independent of its major lamellipodial activator, WRC.

273 Next, we asked whether or to which extent lamellipodia protrusion was affected. To this end,

274 we recorded wild-type, EVM-KO and VASP-reconstituted cells randomly migrating on

275 laminin, and determined respective protrusion rates by kymograph analyses (*Figure 5G-H*,

276 *Figure 5-video 1)*. Quantification revealed lamellipodia protrusion to be reduced by 35% in

277 EVM-KO cells as compared to control or EVM-KO rescued with EGFP-VASP (*Figure 5I*).

278 Notably, despite reduced protrusion, lamellipodia persistence was at best slightly reduced in

279 EVM-KO cells, but not in a statistically significant fashion (*Figure 5J*), confirming that

280 protrusion effectivity can be readily uncoupled from persistence (Block et al., 2012; Kage et

281 al., 2017).

282 Ena/VASP proteins are potent actin polymerases (Breitsprecher et al., 2011a, 2008; Hansen

283 and Mullins, 2010), implying that these factors could affect dynamics of actin assembly in

284 lamellipodia. To test this experimentally, we assessed lamellipodial actin network assembly

285 rates in wild-type and EVM-KO cells (*Figure 5K*, *Figure 5-video 2*). Lamellipodial actin

286 network translocation was also reduced by about 22% in EVM-KO as compared to B16-F1

287 controls, suggesting that the effects on protrusion described above can be explained, at least

288 in part, by reduced actin network polymerization (*Figure 5L*).

289

290 **Loss of Ena/VASP deteriorates lamellipodium architecture**

291 To gain quantitative insights into the ultrastructural details of lamellipodial architecture at the

292 single filament level, we employed three-dimensional (3D) electron microscopy of negatively

293 stained B16-F1 wild-type and EVM-KO samples, allowing computer-assisted tracing of

294 single filaments in 3D space (Mueller et al., 2017; Winkler et al., 2012). Consistent with actin

295 assembly in lamellipodia tips (Lai et al., 2008), filaments are oriented with their barbed ends

296 facing the membrane (Narita et al., 2012). In analogy to recent work (Mueller et al., 2017),

297 barbed ends were scored in digitalized tomograms as the ends of filaments proximal to the

298 leading edge and pointed ends as those distal to the leading edge. Barbed ends either

299 represent actively growing or capped filaments, whereas pointed ends designate Arp2/3

300 complex-generated branch sites, severed or debranched filaments. In contrast to lamellipodia

301   of wild-type cells, EVM-deficient lamellipodia contained much sparser and less organized

302   filament networks (***Figure 6A***, ***Figure 6-video 1***), which is consistent with the F-actin

303   stainings in Figure 3A-B. Consistently, assessment of actin filaments in the front region

304   (within a ~1μm broad zone behind the edge) revealed considerably shorter filaments in the

305   mutant (***Figure 6B***). Moreover, towards the interior of the lamellipodium, filament density in

306   the EVM-mutant decreased noticeably faster as compared to control, while at the edge,

307   barbed ends occurred in excess in the mutant (***Figure 6C***). Consistent with reduced filament

308   lengths (***Figure 6B***) and increased Arp2/3 intensities at the edge of EVM-KO cells (***Figure***

309   ***A-B***), assessed pointed end densities were significantly above control values in particular

310   within the first half micron of the edge (***Figure 6C***). Finally, although both control and

311   mutant lamellipodia exhibited a wide array of filament angles abutting the protruding front,

312   with a clear maximum around 90° relative to the edge (***Figure 6D***), the distribution of

313   filament angles in EVM-deficient lamellipodia was distinct, with the 90° peak being clearly

314   less prominent (17% lower than in control). Conversely, filament fractions with diagonal

315   angles were about doubled compared to controls. These data suggest that reduced filament

316   mass and disordered filament network geometry in the mutant are causative for reduced

317   protrusion and network assembly.

318

319   **Loss of Evl impairs cell spreading and FA formation**

320   To assess Ena/VASP functions in adhesion, we first analyzed spreading of MV^{D7}, derived

321   MVE-KO and reconstituted fibroblasts expressing EGFP-Evl on fibronectin by time-lapse

322   imaging (***Figure 7A, Figure 7-video 1***). Notably, MVE-KO cells displayed a substantial

323   spreading defect that was fully rescued by Evl re-expression (***Figure 7B-C***). Consistent with

324   the removal of Evl in MV^{D7} fibroblasts, B16-F1-derived EVM-KO cells also spread

325   considerably slower than wild-type or reconstituted mutant cells expressing EGFP-tagged

13

326   VASP or Evl (*Figure 7-figure supplement 1A-B*). In these experiments, Evl rescued more

327   effectively compared to VASP (*Figure 7-figure supplement 1C*). Then, we examined FA

328   morphologies in MVE-KO fibroblasts expressing different Ena/VASP family members fused

329   to EGFP. Untransfected MVE-KO cells formed noticeably smaller FAs on average than the

330   same cells expressing distinct Ena/VASP family members, but again, the rescue with Evl

331   appeared most effective (*Figure 7D*). To explore potential effects of Ena/VASP proteins on

332   FA formation more systematically, MV^{D7}, MVE-KO and reconstituted cell lines migrating on

333   fibronectin were labelled for the FA-marker protein vinculin and assessed for various features

334   (*Figure 7E*). Images captured at identical settings were processed by a web-based FA

335   analysis tool (Berginski and Gomez, 2013), allowing a global and unbiased assessment of

336   multiple parameters. Consistent with previous work, untransfected MV^{D7} double-mutant cells

337   still contained prominent FAs (Bear et al., 2000). Notably however, vinculin intensity was

338   clearly reduced in the triple mutant by almost 30% as compared to the parental MV^{D7} cell

339   line, and again fully rescued by Evl expression, while rescue of MVE-KO cells with VASP or

340   Mena was less effective (*Figure 7F*). Consistently, FA size in MVE-KO cells was reduced

341   by 18% as compared to MV^{D7} cells (*Figure 7G*), despite the low abundance of Evl in this cell

342   line (*Figure 2J*). Furthermore, expression of VASP or Mena in MVE-KO cells increased FA

343   size only by 11% or 16%, respectively, while expression of Evl increased FA size by more

344   than 24%. Accordingly, Evl expression was most efficient in rescuing the average number of

345   FAs per cell as compared to VASP and Mena (*Figure 7H*). Together, despite clearly

346   overlapping functions of Ena/VASP proteins in various actin-dependent processes, Evl

347   appeared more critical in the regulation of focal adhesions than VASP or Mena.

348

349   **Loss of Evl diminishes generation of traction forces**

350   Since Evl proved most effective in rescuing parameters addressing FA properties, we finally

351   explored the functional consequence of Evl function in traction force development. To

352   compare traction forces exerted onto a polyacrylamide substratum independently of cell size

353   and geometry, MV^{D7}, MVE-KO cells, and reconstituted cells expressing EGFP-Evl were

354   grown on top of crossbow-shaped micropatterns coated with fibronectin (Vignaud et al.,

355   2014) (*Figure 8A*). Interestingly, the contractile energy was significantly reduced in MVE-

356   KO cells as compared to MV^{D7} (*Figure 8B-C*), and rescued upon stable expression of EGFP-

357   tagged Evl (*Figure 8D-E*). Moreover, the contractile energies of Evl-rescued MVE-KO and

358   parental MV^{D7} cells were highly similar to each other. Comparable results were obtained with

359   unconfined cells, i.e. homogenous fibronectin coating on polyacrylamide substrata, and thus

360   in the absence of size- and geometry-specific constrains (*Figure 8-figure supplement 1A-B*).

361

Discussion

363   In contrast to earlier studies (Bear et al., 2002, 2000), we show that Ena/VASP actin

364   polymerases positively regulate cell migration, since their consecutive loss in B16-F1 cells

365   results in cumulative, reconstitutable motility phenotypes. Thus, despite increased

366   directionality, the reduced net cell translocation rates observed in EVM-KOs as compared to

367   wild-type occur because of reduced lamellipodial actin assembly and protrusion rates.

368   Diminished migration was also observed in MV^{D7} fibroblasts after genetic removal of Evl as

369   well as in NIH 3T3 fibroblast after consecutive disruption of Mena and VASP, supporting the

370   view that Ena/VASP operate in a mechanistically conserved fashion, reconciling previous

371   controversies (Auerbuch et al., 2003; Geese et al., 2002; Loisel et al., 1999; Rottner et al.,

372   1999). But how can these discrepancies be explained? Firstly, MV^{D7} cells proved to be an

373   excellent tool in the field for over two decades now, but were largely considered to be

374   Ena/VASP-free, which we here show not to be the case. Secondly, the concept of Ena/VASP-

15

375   proteins antagonizing efficient cell motility in fibroblasts was largely developed further by

376   inactivating these proteins in Rat2 cells through mitochondrial sequestration *versus* activating

377   them through CAAX-mediating targeting to the plasma membrane (Bear et al., 2002). It was

378   clearly shown in previous studies that mitochondrial sequestration of actin-binding proteins

379   can co-recruit multiple additional interactors of such factors (Fradelizi et al., 2001), so the

380   specificity of this approach for Ena/VASP proteins might be worth reconsidering.

381   Furthermore, it is certainly worth noting that targeting through the general, isoprenylation-

382   prone motif derived from small GTPases, the so called CAAX-box, is a very efficient means

383   of targeting proteins to plasma membranes, but those membranes cannot be equalized to

384   physiological accumulation of Ena/VASP proteins at the membrane, such as focal adhesions

385   as well as tips of lamellipodia and filopodia (Rottner et al, 1999; Svitkina et al., 2003). In this

386   respect, we should emphasize not to question the experimental outcome of previously

387   published data. We should rather emphasize instead that previously employed approaches

388   cannot be directly compared to the loss of function approaches developed here.

389   In line with markedly diminished migration, EVM-KO cells display aberrant, narrow

390   lamellipodia with reduced F-actin densities, shorter filaments and perturbed network

391   geometry. Nevertheless, we should stress the fact that for many years, it had remained

392   unclear in the community whether or not Ena/VASP proteins were essential for the formation

393   of lamellipodial actin networks, which we are clearly able to clarify here not to be the case.

394   But what are the precise consequences of loss of Ena/VASP activity in those lamellipodia

395   still formed in their absence? Interestingly, lamellipodial accumulation of Arp2/3 complex,

396   CP and cortactin is markedly enhanced upon Ena/VASP removal. While CP and cortactin

397   localization frequently coincides with Arp2/3 complex, the latter has indeed already been

398   observed to be negatively correlated with Ena/VASP function (Samarin et al., 2003). Thus, it

399   is tempting to speculate that loss of processive filament elongation upon Ena/VASP removal

16

400   can also increase capping of filaments and Arp2/3 complex-mediated, lamellipodial

401   branching activity (Samarin et al., 2003). This would also be consistent with shorter and more

402   highly branched filaments observed by platinum replica EM upon mitochondrial Ena/VASP

403   sequestration (Bear et al., 2002). Future cryo-EM tomography studies will be required to

404   assess in 3D to what extent increased Arp2/3 complex intensities found in EVM-KOs indeed

405   correlate with enhanced branching.

406   Nevertheless, EVM-KO cells are still capable of impaired lamellipodia formation and

407   migration, raising the question of alternative actin polymerases partly taking over. Previous

408   studies have implicated formins in lamellipodia protrusion in B16-F1, including mDia2

409   (Yang et al., 2007) and FMNL 2 and -3 (Kage et al., 2017). Indeed, FMNL2/3 removal

410   caused defects partly reminiscent of what's seen here, at least concerning impact on

411   lamellipodial protrusion, actin filament densities or microspike formation (see below),

412   although phenotypes seen upon Ena/VASP deficiency were much more severe. Thus, the

413   extent of potential redundancy between all these factors will only be revealed by systematic,

414   combinatorial loss of function studies and side-by-side, phenotypic comparison (Young et al.,

415   2018). Derived conclusions will also have to consider the exciting, recently discovered

416   'distributive polymerase' activity ascribed to WAVE (Bieling et al., 2018).

417   As yet, authors of even highly relevant literature have decided not to clearly distinguish

418   between filopodia and microspikes to facilitate analyses of finger-like protrusions (Svitkina et

419   al., 2003; Vignjevic et al., 2006). However, the virtual absence of microspikes, but not of

420   filopodia, in EVM-KO cells combined with the inability of established filopodia inducers

421   such as mDia2, FMNL3, Myosin X and Rif to rescue microspikes clearly establishes, perhaps

422   for the first time fundamental differences between these molecular entities. The mechanisms

423   underlying filopodia assembly are still under debate: In the convergent elongation model,

424   filopodia form by coalescence of lamellipodial filaments (Svitkina et al., 2003), whereas the

17

425   *de novo* nucleation model proposes filopodia to arise independently of lamellipodial actin

426   networks, as effected by formin-mediated filament nucleation and elongation (Faix et al.,

427   2009; Mellor, 2010). The findings provided here strongly suggest that in contrast to filopodia,

428   microspikes form exclusively by convergent elongation, as previously suggested (Svitkina et

429   al., 2003), whereas filopodia may emerge by multiple, distinct mechanisms (Young et al.,

430   2015), resolving a long-standing controversy in the field.

431   Ena/VASP proteins are well established to accumulate in FAs of adherent cells, and known to

432   reside in the force transduction layer in-between talin and ends of stress fiber filaments

433   (Kanchanawong et al., 2010). However, the presence of multiple orthologues and analyses of

434   only partially-depleted cells hitherto prevented careful functional assessment of their precise

435   contributions to integrin-dependent adhesion. Here we show that lack of Ena/VASP proteins

436   consistently impairs integrin-dependent spreading and changes in FA patterns. Moreover,

437   reduction of adhesion size and adhesion component intensity observed in fibroblasts well

438   correlates with diminished traction forces upon Ena/VASP protein disruption. This clearly

439   illustrates the positive regulatory function of Ena/VASP family members in adhesion

440   formation and exertion of traction forces onto the substratum. The particularly important role

441   of Evl in integrin-dependent adhesion is consistent with very recent work showing its specific

442   requirement for FA maturation, cell-matrix adhesion and mechanosensing (Puleo et al.,

443   2019).

444   Finally, we have not only sought to interpret all our phenotypes in the context of various

445   combinations of gene deletions employing up to three distinct cell types, but also assessed

446   their expression levels in different cell types relative to each other, which certainly adds an

447   additional layer of complexity. Two major points worth being more systematically followed

448   in the future are worth mentioning here. First, Mena is by far the most abundant protein

449   present in both melanoma and fibroblast cell lines, but in particular considering this fact,

450   phenotypes generated by its depletion are comparably modest. In spite of its abundance, we

451   are tempted to speculate therefore that it simply does not sufficiently find its relevant,

452   specific interactors that might promote its impact in other structures such as cell-cell contacts

453   (Scott et al., 2006) or tissues like the nervous system (Kwiatkowski et al., 2007). Finally,

454   given their comparably low abundance, VASP, and in particular Evl, are displaying

455   surprisingly significant relevance in lamellipodia protrusion and adhesion formation,

456   respectively, the molecular nature of which also remains to uncovered in future projects.

457

458   **Materials and methods**

459   **Constructs**

460   cDNAs encoding murine VASP (isoform 1), Mena (isoform 2), and Evl (isoform 2) were

461   amplified by PCR from a NIH 3T3 cDNA library and ligated into suitable sites of pEGFP-C1

462   (Clontech, Palo Alto, CA). VASP cDNA was additionally inserted into the BglII and SalI

463   sites of pmCherry (Addgene ID: 632524). For generation of stably transfected cell lines, the

464   1.3 kb Puro cassette was amplified by PCR using pPur (Clontech) as template and inserted

465   into the Asp718 and BamHI sites of pEGFP-C1 to yield pEGFP-C1 Puro. Subsequently, the

466   cDNA fragment encoding Evl was inserted into the BspEI and XhoI sites of pEGFP-C1 Puro.

467   For generation of constitutively active murine mDia2 (Drf3) lacking the C-terminal

468   regulatory DAD domain (1-1.036), the corresponding cDNA fragment was amplified from a

469   NIH 3T3 cDNA library and inserted into the BspEI and Asp718 sites of pEGFP-C1. Plasmids

470   pEGFP-C1 Lifeact-EGFP (Riedl et al., 2008), pEGFP-Rif-L77 (Aspenström et al., 2004),

471   pEGFP-MyoX (Berg and Cheney, 2002), EGFP-FMNL2-E272 and EGFP-FMNL3-E275

472   (Kage et al., 2017) and pEGFP-fascin (Adams and Schwartz, 2000) have been described.

473   pEGFP-βActin was from Clontech. For generation of recombinant antigens, respective

474   sequences encoding for murine Evl (1-414), VASP (1-375), Mena (1-241), and WAVE2-

19

475   WCA (419-497) were amplified from plasmid DNA and inserted into BamHI/SalI sites of

476   pGEX-6P-1 (GE Healthcare, Munich, Germany). Plasmids pGEX-6P-2-cortactin (Lai et al.,

477   2009) and pGEX-6P-1-fascin (Breitsprecher et al., 2011b) have been described. Fidelity of

478   generated plasmids was confirmed by sequencing.

479

480   **Cell culture and transfection**

481   B16-F1 mouse melanoma cells (CRL-6323) and mouse embryonic NIH 3T3 fibroblast (CRL-

482   1658) were purchased from ATCC. The mouse embryonic fibroblasts cell line MV^{D7}, which

483   expresses a temperature-sensitive version of large T antigen, was derived from Mena/VASP-

484   deficient mice (Bear et al., 2000). For this study, MV^{D7} cells were additionally immortalized

485   with a SV40 wild-type variant of large T antigen-transducing retrovirus by standard

486   procedures, to allow cultivation at 37°C. Expression of Evl in original and derived MV^{D7}

487   cells, immortalized with SV40 wild-type large T antigen, was not affected as assessed by

488   immunoblotting (data not shown). B16-F1, NIH 3T3 and immortalized MV^{D7} cells were

489   cultured at 37°C and 5% CO_2 in high glucose DMEM culture medium (Lonza, Cologne,

490   Germany) supplemented with 10% FBS (Biowest), 2 mM UltraGlutamine (Lonza) and 1%

491   Penicillin-Streptomycin (Biowest). B16-F1 cells were transfected with 1 μg plasmid DNA

492   and MV^{D7} and NIH 3T3 cells with 3 μg plasmid DNA, respectively using JetPRIME

493   transfection reagent (PolyPlus, Illkirch, France) in 35 mm diameter wells (Sarstedt,

494   Nümbrecht, Germany) according to the manufacturer's protocol. Absence of mycoplasma in

495   cell lines was routinely checked by the VenorGeM Mycoplasma Detection Kit (Sigma, St.

496   Louis, MO).

497

498   **Genome editing by CRISPR/Cas9**

20

499   DNA target sequences were pasted into CRISPR/Cas9 design tool (http://crispr.mit.edu/) to

500   generate sgRNAs of 20 nucleotides with high efficiency scores. In case of Evl, the targeting

501   sequence 5'-GATCGGTACCCACTTCTTAC-3' was used to cover all possible splice

502   variants. Accordingly, genome editing of VASP was performed with 5'-

503   GTAGATCTGGACGCGGCTGA-3', and for disruption of Mena expression, the sgRNA 5'-

504   AAGGGAGCACGTGGAGCGGC-3' was used. Respective sequences were ligated into

505   expression plasmid pSpCas9(BB)-2A-Puro(PX459)V2.0 (Addgene plasmid ID: 62988) using

506   BbsI (Ran et al., 2013). Validation of CRISPR construct sequences was performed using a 5'-

507   GGACTATCATATGCTTACCG-3' sequencing primer. 24 h after transfection with the

508   CRISPR constructs, cells were selected in culture medium containing puromycin (B16-F1: 2

509   µg/mL, MV^{D7}: 4 µg/mL and NIH 3T3: 5 µg/mL) for 4 days, and then cultivated for 24 h in

510   the absence of puromycin. For isolation of clonal knockout cell lines, single cells were seeded

511   by visual inspection into 96 well microtiter plates and expanded in pre-conditioned culture

512   medium containing 20% BriClone supplement (NICB, Dublin City University, Ireland).

513   Clones were analyzed by the TIDE sequence trace decomposition web tool

514   (https://tide.deskgen.com/, (Brinkman et al., 2014)) and immunoblotting using specific

515   antibodies, and subsequently verified by sequencing (*Supplementary file 1*). For the latter,

516   respective DNA fragments of about 500 bp encompassing the target sites were first amplified

517   from genomic DNA using the Evl primer combination 5'-AAGCCATGAGTCTCCCAAGC-

518   3' and 5'-GTCTCACGCTTTGGCTCTCA-3', the VASP primer combination 5'-

519   GTGTGGCCTGCCTATCTGTT-3' and 5'-CAGAGGGACAGAGGGACAGA-3', and the

520   Mena primer pair 5'-TCAGGCAACTGCAAGAACAG-3' and 5'-

521   CATCTCGGCTGTAGGAGGTG-3'. Subsequently, amplified fragments were inserted into

522   pJet1.2 vector (Thermo Fisher Scientific, Carlsbad, CA) and used for transformation of *E.*

21

523   *coli* host DH5α (Thermo Fisher Scientific). At least 30 sequences were analyzed for each

524   knockout clone.

525

526   **Generation of recombinant proteins and antibodies**

527   For expression of recombinant proteins, the *E. coli* strain Rossetta 2 (Novagen) was used.

528   Expression of GST-tagged fusion proteins was induced using 1 mM isopropyl-ß-D-

529   thiogalactoside (IPTG) (Carl Roth, Karlsruhe, Germany) at 21°C for 14 h. Purification of

530   respective proteins from bacterial extracts was performed by affinity chromatography using

531   Protino glutathione-conjugated agarose 4B (Macherey-Nagel, Düren, Germany). Except for

532   GST-WAVE2-WCA, the GST-tag was removed by proteolytic cleavage with PreScission

533   Protease (GE Healthcare), followed by a final polishing step of the proteins by size-exclusion

534   chromatography on an Äkta Purifier System using either HiLoad 26/600 Superdex 200 or

535   HiLoad 26/75 Superdex columns (GE Healthcare). Purified proteins were dialyzed against

536   immunization buffer (150 mM NaCl, 1 mM dithiothreitol (DTT), and 20 mM Tris/HCl pH

537   7.4) and stored in aliquots at -20°C. Polyclonal antibodies against Evl, VASP, Mena,

538   cortactin and WAVE2 were raised by immunizing New Zealand white rabbits with respective

539   recombinant proteins following standard procedures. Evl, Mena and cortactin polyclonal

540   antibodies were subsequently purified by affinity chromatography using antigens conjugated

541   to sepharose. GST antibodies in the anti GST-WAVE2-WCA serum were absorbed by GST-

542   affinity chromatography. Monoclonal antibodies against fascin were produced upon injecting

543   recombinant fascin mixed with CpG-DNA as adjuvant (*Magic Mouse*, Creative, NY, USA)

544   into 7 week-old, female mice (Charles River, USA) using standard hybridoma technology

545   and antibody screening procedures in the PROCOMPAS graduate programme-funded

546   monoclonal antibody facility (Braunschweig Integrated Centre of Systems Biology - BRICS,

547   Technische Universität Braunschweig). Hybridoma clone 5E2 was selected and kindly

548   provided by Sabine Buchmeier and Prof. Dr. em. Brigitte Jockusch (TU Braunschweig).

549

550   **Antibodies used**

551   Immunoblotting was performed according to standard protocols using rabbit polyclonal

552   antibodies directed against Evl (1:1000 dilution), VASP (1:1000 dilution), Mena (1:1000

553   dilution), WAVE2 (1:1000 dilution), GFP (1:2000) (Faix et al., 2001) or mouse monoclonal

554   antibody against glyceraldehyde-3-phosphate dehydrogenase (GAPDH) (1:1000; #CB1001-

555   500UG, Merck (Darmstadt, Germany)) and anti-fascin antibody 5E2 (undiluted hybridoma

556   supernatant). Primary antibodies in immunoblots were visualized using phosphatase-coupled

557   anti-mouse (1:1,000 dilution; #115-055-62, Dianova (Hamburg, Germany)) or anti-rabbit

558   antibodies (1:1,000 dilution; #115-055-144, Dianova). For immunofluorescence, the

559   following primary antibodies were used: rabbit anti-cortactin antibodies (1:1000 dilution),

560   mouse monoclonal anti-fascin antibody 5E2 (undiluted hybridoma supernatant), mouse

561   monoclonal anti-ArpC5A (p16-ArcA) from hybridoma culture clone 323H3 (Olazabal et al.,

562   2002), mouse monoclonal anti-capping protein α1/α2 subunits (hybridoma supernatant; 1:4

563   dilution; Developmental Hybridoma Bank, University of Iowa, Iowa City, IA) and mouse

564   monoclonal anti-vinculin antibody (1:1,000 dilution, #V9131, clone hVIN-1, Sigma).

565   Primary antibodies were visualized in immunohistochemistry with polyclonal Alexa-555-

566   conjugated goat-anti-rabbit (1:1,000 dilution; #A21429, Invitrogen (Carlsbad, CA)) or goat-

567   anti-mouse (1:1,000 dilution, #A32727, Invitrogen) and Alexa-488-conjugated goat-anti-

568   rabbit (1:1,000 dilution; #A-11034, Invitrogen) or goat-anti-mouse antibodies (1:1,000

569   dilution; #A-11029, Invitrogen). To enhance EGFP signals, Alexa488-conjugated nanobodies

570   from Chromotek (Chromotek, (Planegg-Martinsried, Germany)) (1:200 dilution; #gba488)

571   were used. Atto550-phalloidin (1:250 dilution, #AD 550-82, Atto-Tec (Siegen, Germany))

572   was used for visualization of F-actin.

573

574   **Immunoblotting**

575   For preparation of total cell lysates, cells were cultured to confluency and trypsinized. Cell

576   pellets were washed twice with cold PBS and lysed with cold RIPA buffer (150 mM NaCl,

577   1.0% Triton X-100, 0.5% sodium deoxycholate, 0.1% sodium dodecyl sulfate (SDS), 50 mM

578   Tris, pH 8.0) supplemented 5 mM benzamidine (Carl Roth), 0.1 mM AEBSF (AppliChem,

579   Darmstadt, Germany) and Benzonase (1:1000, Merck) for 1 h at 4°C on a wheel rotator. Cell

580   lysates were subsequently homogenized by passing the lysate 10 times through a syringe

581   cannula (Braun). Protein contents of total cell lysates were determined by Pierce BCA assay

582   (Thermo Fisher Scientific) using a Synergy 4 fluorescence microplate reader (Biotek, Bad

583   Friedrichshall, Germany) according to manufacturer's protocol. 50 μg (B16-F1) or 100 μg

584   (MEF) of total proteins per lane were subjected to SDS-PAGE, and transferred by semi-dry

585   blotting onto nitrocellulose membranes (Hypermol, Hannover, Germany). Blotting

586   membranes were then blocked with NCP buffer (10 mM Tris/HCL, 150 mM NaCl, 0.05%

587   Tween-20, 0.02% NaN_3, pH 8.0,) containing 4% bovine serum albumin (BSA) for 1 h and

588   incubated with primary antibodies overnight in the same buffer. After extensive washing of

589   membranes and incubation with secondary, phosphatase-conjugated antibodies for at least 2

590   hours, blots were developed with 20 mg/mL of 5-brom-4-chlor-3-indolylphosphat-p-toluidin

591   (BCIP) in $NaHCO_3$, pH 10.0.

592

593   **Quantification of cellular Ena/VASP protein concentrations**

594   Total cellular concentrations of Ena/VASP family members in used cell lines were quantified

595   from immunoblots using orthologue-specific antibodies by titrating total cell lysates

24

596   corresponding to a defined number of B16-F1, NIH 3T3 and MVD7 cells with dilution series

597   containing defined amounts of recombinant proteins loaded on the same gels. Band

598   intensities were quantified by ImageJ software. The cell volume for each cell type was

599   calculated from phase-contrast images of freshly trypsinized, non-adherent cells (>50 for

600   each cell line). The volume of the nucleus was subtracted from the cell volume to obtain the

601   volume of the cytoplasm.

602

603   **Live cell imaging**

604   Time-lapse imaging of cells was performed using an Olympus XI-81 inverted microscope

605   (Olympus, Hamburg, Germany) driven by Metamorph software (Molecular Devices, San

606   Jose, CA) and equipped with objectives specified below and a CoolSnap EZ camera

607   (Photometrics, Photometrics, Tucson, AZ). Cells were seeded onto 35 mm glass bottom

608   dishes (Ibidi, Planegg-Martinsried, Germany) coated with either 25 µg/mL laminin (Sigma)

609   in case of B16-F1 cells and derived clones, or with 10 µg/mL fibronectin (Roche, Penzberg,

610   Germany) in case of MV^{D7}, NIH 3T3 and their derivatives, and maintained in imaging

611   medium composed of F-12 Ham Nutrient Mixture with 25 mM HEPES (Sigma), the latter to

612   compensate for the lack of CO_2, and supplemented with 10% FBS (Biowest, Nuaillé, France),

613   1% Penicillin-Streptomycin (Biowest), 2 mM stable L-glutamine (Biowest), and 2.7 g/L D-

614   glucose (Carl Roth) in an Ibidi Heating System at 37 °C. For random motility assays, B16-

615   F1cells were seeded at low density onto the dishes and allowed to adhere for 3 h.

616   Subsequently, the medium was exchanged with imaging medium, the chamber mounted into

617   a heating system, and cells recorded by time-lapse phase-contrast imaging at 60 sec intervals

618   for 3 h using an Uplan FL N 4x/0.13NA objective (Olympus). NIH 3T3, MV^{D7} and derived

619   cells were allowed to settle for 6 h after seeding and imaged at 10 min intervals for 10 h using

620   an UPlan FL N 10x/0.30NA objective (Olympus). Single cell tracking was performed in

25

621 ImageJ by MTrackJ. Analyses of cell speed and cell trajectories, turning angles, and mean

622 square displacements were performed in Excel (Microsoft, Redmond, WA) using a

623 customized macro (Litschko et al., 2018). Cells that contacted each other or divided were

624 excluded from analyses. Directionality index ratio was determined by dividing the shortest

625 distance between starting and end points (d) by the actual trajectories (D). For wound healing

626 assays, MV^{D7} cells were seeded onto uncoated dishes and expanded to confluency.

627 Subsequently, the monolayer was scratched with a 200 μL pipette tip, the cells washed three

628 times with warm imaging medium, and recorded by phase-contrast time-lapse imaging at 10

629 min intervals for 20 h using an UPlan FL N 10x/0.30NA objective (Olympus). Wound

630 closure rates were determined in ImageJ by measuring decrease of scratch area over time.

631 Lamellipodial protrusions were recorded at 5 sec intervals for 10 min using an UPlan FL

632 40x/0.75NA objective (Olympus). Protrusion rates of advancing lamellipodia assessed over a

633 time period of 2.5 min were quantified by first generating kymographs from time-lapse

634 movies of the cell periphery using ImageJ, followed by slope determination from these

635 kymographs. Lamellipodial persistence of randomly migrating B16-F1 and derived cells on

636 laminin was determined by phase-contrast time-lapse microscopy using an UPlan FL N

637 10x/0.30NA objective and a frame rate of 1 frame per minute. Lamellipodial persistence was

638 defined as time in min from initiation till collapse of the lamellipodium. Spreading of B16-F1

639 and derived clones was monitored at 30 sec intervals by time-lapse phase-contrast imaging

640 for 30 min using an UPlan FL N 10x/0.30NA objective immediately after seeding, and

641 spreading of MV^{D7} and derived lines were imaged at 30 sec intervals for 1 h using an

642 Olympus LUCPlan FL N 20x/0.45NA objective. Quantification of cell spreading was

643 executed with ImageJ from time-lapse movies by measuring increase of cell area over time.

644 For epifluorescence imaging of fluorescently-labelled cells, B16-F1, EVM-KO and

645 reconstituted EVM-KO cells expressing mCherry-VASP were transfected with either

646   pEGFP-Lifeact or pEGFP-fascin. 24 h post transfection, cells were seeded into imaging

647   medium, and after 3 h, migrating cells recorded by time-lapse imaging at 10 sec intervals for

648   10 min using an Olympus 40x/0.75NA Uplan FL objective. In motility and spreading assays,

649   reconstituted cells expressing EGFP-tagged VASP, Evl or Mena were identified by

650   epifluorescence imaging.

651

Immunofluorescence

653   If not indicated otherwise for immunofluorescence labelling, cells were fixed in pre-warmed,

654   4% PFA in PBS, pH 7.3 for 20 min, subsequently washed three times with PBS

655   supplemented with 100mM glycine, permeabilized with 0.1% Triton X-100 in PBS for 3 min

656   and blocked in PBG (PBS, 0.045% cold fish gelatin (Sigma), and 0.5% BSA). For

657   immunolabeling with fascin, cells were fixed in -20°C cold methanol. For immunolabeling of

658   capping protein, the cells were fixed with 3% glyoxal at pH 5.0 as described (Richter et al.,

659   2018) and then treated as above. To reduce cytoplasmic background in vinculin stainings,

660   cells were fixed for 1 min with 2% PFA in PBS containing 0.3% Triton X-100 and then

661   postfixed with 4% PFA in PBS for 20 min as described (Kage et al., 2017). Primary

662   antibodies were incubated overnight, followed by extensive washing of the specimens with

663   PBG and incubation with respective secondary antibodies for at least 2 h. GFP signals were

664   enhanced with Alexa488-conjugated nanobodies. F-actin was visualized with Atto550

665   phalloidin. Imaging of fixed cells was performed with an Olympus XI-81 inverted

666   microscope equipped with an UPlan FI 100x/1.30NA oil immersion objective or an LSM510

667   Meta confocal microscope (Carl Zeiss, Jena, Germany) equipped with a Plan-Neofluar

668   63x/1.3NA oil immersion objective using 488 nm and 543 nm laser lines.

669   Fluorescence intensities of phalloidin or lamellipodial proteins were measured from still

670   images captured at identical settings using ImageJ software after background subtraction.

27

671   Mean pixel intensities in lamellipodial regions of interest are shown as whiskers-box plots

672   including all data points.

673

Induction of filopodia in absence of lamellipodia

675   B16-F1 wild-type and EVM-KO cells were seeded onto low laminin (1µg/mL) for 1 h, a

676   concentration lower than the threshold for inducing prominent lamellipodia in this cell type

677   and conditions (data not shown). Then, the cells were incubated for 2 h with the Arp2/3

678   complex inhibitor CK666 (200 µM) to completely abolish lamellipodia and trigger filopodia

679   formation. Subsequently, cells were fixed and stained with phalloidin for the actin

680   cytoskeleton followed by confocal imaging.

681

Determination of actin assembly rates in lamellipodia

683   Quantification of lamellipodial actin polymerization rates were performed in B16-F1 and

684   EMV-KO cells transiently expressing EGFP-ß-actin, by photobleaching protruding

685   lamellipodial regions and subsequently measuring the distance of fluorescence recovery from

686   the lamellipodium tip over time, essentially as described (Dimchev and Rottner, 2018). In

687   brief, photobleaching of EGFP-ß-actin was accomplished on an epi-FRAP system, equipped

688   with a 405-nm diode laser (settings: 65 mW laser power, 10-pixel laser beam diameter, 1ms

689   bleach dwell time/pixel), which was manually triggered in selected regions during image

690   acquisition (exposure time of 500 ms). Time-lapse imaging was performed with an interval of

691   1.5 sec between frames. Images were acquired with a 100x/1.4NA Plan apochromatic oil

692   immersion objective on an inverted Axio Observer (Carl Zeiss, Jena, Germany) using a DG4

693   light source (Sutter Instrument, Novato, CA) for epifluorescence illumination and a

694   CoolSnap-HQ2 camera (Photometrics, Tucson, AZ), driven by VisiView software (Visitron

695   Systems, Puchheim, Germany).

696

Electron tomography

697

698 B16-F1 and EMV-KO cells were grown on Formvar-coated copper-palladium grids coated

699 with 25 μg/mL laminin (Sigma) in laminin coating buffer (150 mM NaCl, 50 mM Tris, pH

700 7.5). The cells were simultaneously extracted and fixed for 1 min with 0.5% Triton X-100

701 (Fluka, Buchs, Switzerland) and 0.25% glutaraldehyde (Agar Scientific, Stansted, United

702 Kingdom) in cytoskeleton buffer (10 mM MES buffer, 150 mM NaCl, 5 mM EGTA, 5 mM

703 glucose and 5 mM $MgCl_2$, pH 6.1), followed by a second fixation step for 15 minutes in

704 cytoskeleton buffer (pH 7.0) containing 2% glutaraldehyde. The coverslips were incubated

705 for additional 4-12 h in cytoskeleton buffer containing 2% glutaraldehyde at 4°C, and were

706 then stained for electron microscopy. Negative staining was performed in mixtures of 4-6%

707 sodium silicotungstate (Agar Scientific) at pH 7.0, containing 10 nm gold colloid saturated

708 with BSA, and diluted 1:10 from a gold stock (Urban et al., 2010). Double tilt series of

709 negatively stained cytoskeletons were acquired on a FEI Tecnai G20 transmission electron

710 microscope (Tecnai, Hillsboro, OR) operated at 200 kV driven by SerialEM 3.x

711 (Mastronarde, 2005) equipped with an Eagle 4k HS CCD camera (Gatan, Pleasanton, CA).

712 Double axis tilt series were acquired with typical tilt angles from -65° to +65° and 1°

713 increments following the Saxton scheme at a primary on-screen magnification of 25,000x.

714 Actin filaments were tracked automatically using a Matlab-based tracking algorithm (Mueller

715 et al., 2017; Winkler et al., 2012).

716

Focal adhesion analysis

717

718 Focal adhesions in MV^{D7} and derived cells were analyzed from confocal images captured at

719 identical settings. Images of cells labelled for vinculin were first processed in ImageJ by

720 background subtraction using a rolling ball radius of 40 pixels, exclusion of nuclear regions

29

721   due to high background staining, and by contouring of cell perimeters. Preprocessed images

722   were then analyzed by the Focal Adhesion Analysis Server (Berginski and Gomez, 2013).

723   The parameters were set to imaging frequency 0 min, detection threshold 3.5 and minimal

724   adhesion size of 10 pixels. Obtained values for FA intensity and size as well as number of

725   FAs/cell were subsequently analyzed in Excel.

726

727   **Traction force analysis**

728   Patterned polyacrylamide hydrogels were fabricated according to the Mask method (Vignaud

729   et al., 2014). A quartz photomask was first cleaned through oxygen plasma (AST product,

730   300W) for 3.5 min at 200 W. Areas containing crossbow patterns were then incubated with

731   0.1 mg/mL Poly(L-lysine)-graft-poly(ethylene glycol) (PLL-g-PEG) (JenKem Technology,

732   Plano, TX) in 10mM HEPES, pH 7.4 for 30 min. After a rapid de-wetting step, PLL-PEG

733   was burned using deep-UV exposure for 6 min. Patterns on the mask were then incubated

734   with a mix of 10 µg/mL fibronectin (Sigma) and 10 µg/mL fibrinogen Alexa Fluor 647

735   conjugate (Invitrogen) in 100 mM sodium bicarbonate buffer pH, 8.4 for 30 min. A mix of

736   8% acrylamide (Sigma) and 0.264% bis-acrylamide solution (Sigma) was degassed for 30

737   min, mixed with 0.2 µm diameter PLL-PEG-coated fluorescent beads (Fluorosphere #F8810,

738   Life Technologies (Carlsbad, CA)) and sonicated before addition of APS and TEMED. 25 µL

739   of this solution was added onto the micropatterned photomask, covered with a silanized

740   coverslip, and allowed to polymerize for 25 min before being gently detached in sodium

741   bicarbonate buffer. Micropatterns were stored overnight in sodium bicarbonate buffer at 4°C

742   before plating cells. Non-patterned hydrogels were prepared using the same polyacrylamide

743   polymerization procedure followed by a step of oxygen plasma treatment for 30 sec at 30 W

744   of the coverslips and subsequent incubation with fibronectin for 30 min.

745   For identification of untransfected MVE-KO cells on patterns, the cells were stained with 1

746   µM CellTracker Green (Invitrogen) for 5 min followed by removal of unbound dye with

747   PBS. In case of reconstituted MVE-KO cells, only cells expressing EGFP-Evl that exhibited

748   appropriate localization of the fusion protein at focal adhesions on the patterns were selected

749   for performing traction force experiments. Images were acquired on an EclipseTi-E Nikon

750   confocal spinning disk microscope equipped with a CSUX1-A1 Yokogawa confocal head.

751   Data were analyzed with a set of macros in Fiji (Martiel et al., 2015). Displacement fields

752   were obtained from bead images prior and after removal of cells by trypsin treatment. Bead

753   images were first paired and aligned to correct for experimental drift. Displacement field was

754   calculated by particle imaging velocimetry (PIV) on the base of normalized cross-correlation

755   following an iterative scheme. Erroneous vectors where discarded owing to their low

756   correlation value and replaced by the median value of neighboring vectors. Traction-force

757   field was subsequently reconstructed by Fourier Transform Traction Cytometry, with a

758   regularization parameter set to 3.2×10^{-10}.

759

760   **Statistical analyses**

761   Quantitative experiments were performed at least in triplicates to avoid any potential bias of

762   environmental influences or unintentional error. Impact on lamellipodial or adhesion

763   phenotypes derived from analyses on fixed samples and living cells were systematically

764   obtained from sample sizes of dozens or hundreds of cells, respectively. Raw data were

765   processed in Excel (Microsoft). Statistical analyses were performed using SigmaPlot 11.0

766   software (Systat Software, Erkrath, Germany) or GraphPad Prism 5 (GraphPad, San Diego,

767   CA). All data sets were tested for normality by the Shapiro-Wilk test. Statistical differences

768   between not normally distributed datasets of two groups were determined by the non-

769   parametric Mann-Whitney U rank sum test. For comparison of more than 2 groups, statistical

31

770 significance of normally-distributed data was examined by one-way ANOVA and Tukey

771 Multiple Comparison test. In case of not normally-distributed data, the non-parametric

772 Kruskal-Wallis test and Dunn's Multiple Comparison test were used. Statistical differences

773 were defined as $*p{\leq}0.05$, $**p{\leq}0.01$, $***p{\leq}0.001$ as well as n.s., not significant, and are

774 displayed and mentioned in figures and figure legends, respectively. Graphs were created

775 with Origin 2018G (OriginLab, Northampton, Ma), and final figures prepared with

776 Photoshop (Adobe, San Jose, CA) and CorelDraw Graphics Suite 6X (CorelDraw, Ottawa,

777 On).

778

Acknowledgements

787

788 **Competing interests:** The authors declare that no competing interests exist.

789

References:

790

791 Adams JC, Schwartz MA. 2000. Stimulation of fascin spikes by thrombospondin-1 is

792 mediated by the GTPases Rac and Cdc42. *J Cell Biol* **150**:807–22.

793 doi:10.1083/jcb.150.4.807

794 Aspenström P, Fransson A, Saras J. 2004. Rho GTPases have diverse effects on the

32

795   organization of the actin filament system. *Biochem J* **377**:327–37.

796   doi:10.1042/BJ20031041

797   Auerbuch V, Loureiro JJ, Gertler FB, Theriot JA, Portnoy DA. 2003. Ena/VASP proteins

798   contribute to Listeria monocytogenes pathogenesis by controlling temporal and spatial

799   persistence of bacterial actin-based motility. *Mol Microbiol* **49**:1361–75.

800   Bear JE, Gertler FB. 2009. Ena/VASP: towards resolving a pointed controversy at the barbed

801   end. *J Cell Sci* **122**:1947–1953. doi:10.1242/jcs.038125

802   Bear JE, Loureiro JJ, Libova I, Fässler R, Wehland J, Gertler FB. 2000. Negative regulation

803   of fibroblast motility by Ena/VASP proteins. *Cell* **101**:717–28.

804   Bear JE, Svitkina TM, Krause M, Schafer DA, Loureiro JJ, Strasser GA, Maly I V, Chaga

805   OY, Cooper JA, Borisy GG, Gertler FB. 2002. Antagonism between Ena/VASP proteins

806   and actin filament capping regulates fibroblast motility. *Cell* **109**:509–21.

807   Berg JS, Cheney RE. 2002. Myosin-X is an unconventional myosin that undergoes

808   intrafilopodial motility. *Nat Cell Biol* **4**:246–250. doi:10.1038/ncb762

809   Berginski ME, Gomez SM. 2013. The Focal Adhesion Analysis Server: a web tool for

810   analyzing focal adhesion dynamics. *F1000Research* **2**:68.

811   doi:10.12688/f1000research.2-68.v1

812   Bieling P, Hansen SD, Akin O, Li T, Hayden CC, Fletcher DA, Mullins RD. 2018. WH2 and

813   proline-rich domains of WASP-family proteins collaborate to accelerate actin filament

814   elongation. *EMBO J* **37**:102–121. doi:10.15252/embj.201797039

815   Blanchoin L, Boujemaa-Paterski R, Sykes C, Plastino J. 2014. Actin dynamics, architecture,

816   and mechanics in cell motility. *Physiol Rev* **94**:235–63. doi:10.1152/physrev.00018.2013

817   Block J, Breitsprecher D, Kühn S, Winterhoff M, Kage F, Geffers R, Duwe P, Rohn JL,

818   Baum B, Brakebusch C, Geyer M, Stradal TE, Faix J, Rottner K. 2012. FMNL2 drives

819   actin-based protrusion and migration downstream of Cdc42. *Curr Biol* **22**:1005–12.

33

820   doi:10.1016/j.cub.2012.03.064

821   Block J, Stradal TE, Hänisch J, Geffers R, Köstler SA, Urban E, Small JV, Rottner K, Faix J.

822   2008. Filopodia formation induced by active mDia2/Drf3. *J Microsc* **231**.

823   doi:10.1111/j.1365-2818.2008.02063.x

824   Bohil AB, Robertson BW, Cheney RE. 2006. Myosin-X is a molecular motor that functions

825   in filopodia formation. *Proc Natl Acad Sci* **103**:12411–12416.

826   doi:10.1073/pnas.0602443103

827   Breitsprecher D, Kiesewetter AK, Linkner J, Urbanke C, Resch GP, Small JV, Faix J. 2008.

828   Clustering of VASP actively drives processive, WH2 domain-mediated actin filament

829   elongation. *EMBO J* **27**:2943–2954. doi:10.1038/emboj.2008.211

830   Breitsprecher D, Kiesewetter AK, Linkner J, Vinzenz M, Stradal TEB, Small JV, Curth U,

831   Dickinson RB, Faix J. 2011a. Molecular mechanism of Ena/VASP-mediated actin-

832   filament elongation. *EMBO J* **30**:456–467. doi:10.1038/emboj.2010.348

833   Breitsprecher D, Koestler SA, Chizhov I, Nemethova M, Mueller J, Goode BL, Small JV,

834   Rottner K, Faix J. 2011b. Cofilin cooperates with fascin to disassemble filopodial actin

835   filaments. *J Cell Sci* **124**:3305–3318. doi:10.1242/jcs.086934

836   Brinkman EK, Chen T, Amendola M, van Steensel B. 2014. Easy quantitative assessment of

837   genome editing by sequence trace decomposition. *Nucleic Acids Res* **42**:e168.

838   doi:10.1093/nar/gku936

839   Brühmann S, Ushakov DS, Winterhoff M, Dickinson RB, Curth U, Faix J. 2017. Distinct

840   VASP tetramers synergize in the processive elongation of individual actin filaments

841   from clustered arrays. *Proc Natl Acad Sci* **114**:E5815–E5824.

842   doi:10.1073/pnas.1703145114

843   Dimchev G, Rottner K. 2018. Micromanipulation Techniques Allowing Analysis of

844   Morphogenetic Dynamics and Turnover of Cytoskeletal Regulators. *J Vis Exp*.

845   doi:10.3791/57643

846   Eden S, Rohatgi R, Podtelejnikov A V., Mann M, Kirschner MW. 2002. Mechanism of

847   regulation of WAVE1-induced actin nucleation by Rac1 and Nck. *Nature* **418**:790–793.

848   doi:10.1038/nature00859

849   Faix J, Breitsprecher D, Stradal TE, Rottner K. 2009. Filopodia: Complex models for simple

850   rods. *Int J Biochem Cell Biol* **41**. doi:10.1016/j.biocel.2009.02.012

851   Faix J, Weber I, Mintert U, Köhler J, Lottspeich F, Marriott G. 2001. Recruitment of

852   cortexillin into the cleavage furrow is controlled by Rac1 and IQGAP-related proteins.

853   *EMBO J* **20**:3705–15. doi:10.1093/emboj/20.14.3705

854   Fradelizi J, Noireaux V, Plastino J, Menichi B, Louvard D, Sykes C, Golsteyn RM,

855   Friederich E. 2001. ActA and human zyxin harbour Arp2/3-independent actin-

856   polymerization activity. *Nat Cell Biol* **3**:699–707. doi:10.1038/35087009

857   Galler AB, García Arguinzonis MI, Baumgartner W, Kuhn M, Smolenski A, Simm A,

858   Reinhard M. 2006. VASP-dependent regulation of actin cytoskeleton rigidity, cell

859   adhesion, and detachment. *Histochem Cell Biol* **125**:457–474. doi:10.1007/s00418-005-

860   0091-z

861   Gateva G, Tojkander S, Koho S, Carpen O, Lappalainen P. 2014. Palladin promotes assembly

862   of non-contractile dorsal stress fibers through VASP recruitment. *J Cell Sci* **127**:1887–

863   1898. doi:10.1242/jcs.135780

864   Geese M, Loureiro JJ, Bear JE, Wehland J, Gertler FB, Sechi AS. 2002. Contribution of

865   Ena/VASP proteins to intracellular motility of listeria requires phosphorylation and

866   proline-rich core but not F-actin binding or multimerization. *Mol Biol Cell* **13**:2383–96.

867   doi:10.1091/mbc.e02-01-0058

868   Gertler FB, Niebuhr K, Reinhard M, Wehland J, Soriano P. 1996. Mena, a relative of VASP

869   and Drosophila Enabled, is implicated in the control of microfilament dynamics. *Cell*

870   **87**:227–39.

871   Gupton SL, Anderson KL, Kole TP, Fischer RS, Ponti A, Hitchcock-DeGregori SE, Danuser

872   G, Fowler VM, Wirtz D, Hanein D, Waterman-Storer CM. 2005. Cell migration without

873   a lamellipodium: translation of actin dynamics into cell movement mediated by

874   tropomyosin. *J Cell Biol* **168**:619. doi:10.1083/JCB.200406063

875   Gupton SL, Riquelme D, Hughes-Alford SK, Tadros J, Rudina SS, Hynes RO, Lauffenburger

876   D, Gertler FB. 2012. Mena binds α5 integrin directly and modulates α5β1 function. *J*

877   *Cell Biol* **198**:657–76. doi:10.1083/jcb.201202079

878   Han Y-H, Chung CY, Wessels D, Stephens S, Titus MA, Soll DR, Firtel RA. 2002.

879   Requirement of a Vasodilator-stimulated Phosphoprotein Family Member for Cell

880   Adhesion, the Formation of Filopodia, and Chemotaxis in Dictyostelium. *J Biol Chem*

881   **277**:49877–49887. doi:10.1074/jbc.M209107200

882   Hansen SD, Mullins RD. 2015. Lamellipodin promotes actin assembly by clustering

883   Ena/VASP proteins and tethering them to actin filaments. *Elife* **4**:1–29.

884   doi:10.7554/eLife.06585

885   Hansen SD, Mullins RD. 2010. VASP is a processive actin polymerase that requires

886   monomeric actin for barbed end association. *J Cell Biol* **191**:571–584.

887   doi:10.1083/jcb.201003014

888   Harris ES, Gauvin TJ, Heimsath EG, Higgs HN. 2010. Assembly of filopodia by the formin

889   FRL2 (FMNL3). *Cytoskeleton* **67**:755–772. doi:10.1002/cm.20485

890   Innocenti M, Zucconi A, Disanza A, Frittoli E, Areces LB, Steffen A, Stradal TE, Fiore PP

891   Di, Carlier M-F, Scita G. 2004. Abi1 is essential for the formation and activation of a

892   WAVE2 signalling complex. *Nat Cell Biol* **6**:319–327. doi:10.1038/ncb1105

893   Ismail AM, Padrick SB, Chen B, Umetani J, Rosen MK. 2009. The WAVE regulatory

894   complex is inhibited. *Nat Struct Mol Biol* **16**:561–3. doi:10.1038/nsmb.1587

895   Kage F, Winterhoff M, Dimchev V, Mueller J, Thalheim T, Freise A, Brühmann S, Kollasser

896   J, Block J, Dimchev G, Geyer M, Schnittler H-J, Brakebusch C, Stradal TE, Carlier M-

897   F, Sixt M, Käs J, Faix J, Rottner K. 2017. FMNL formins boost lamellipodial force

898   generation. *Nat Commun* **8**. doi:10.1038/ncomms14832

899   Kanchanawong P, Shtengel G, Pasapera AM, Ramko EB, Davidson MW, Hess HF,

900   Waterman-Storer CM. 2010. Nanoscale architecture of integrin-based cell adhesions.

901   *Nature* **468**:580–584. doi:10.1038/nature09621

902   Kang N, Yaqoob U, Geng Z, Bloch K, Liu C, Gomez T, Billadeau D, Shah V. 2010. Focal

903   Adhesion Assembly in Myofibroblasts Fosters a Microenvironment that Promotes

904   Tumor Growth. *Am J Pathol* **177**:1888–1900. doi:10.2353/ajpath.2010.100187

905   Koestler SA, Auinger S, Vinzenz M, Rottner K, Small JV. 2008. Differentially oriented

906   populations of actin filaments generated in lamellipodia collaborate in pushing and

907   pausing at the cell front. *Nat Cell Biol* **10**:306–13. doi:10.1038/ncb1692

908   Koestler SA, Steffen A, Nemethova M, Winterhoff M, Luo N, Holleboom JM, Krupp J,

909   Jacob S, Vinzenz M, Schur F, Schlüter K, Gunning PW, Winkler C, Schmeiser C, Faix

910   J, Stradal TE, Small JV, Rottner K. 2013. Arp2/3 complex is essential for actin network

911   treadmilling as well as for targeting of capping protein and cofilin. *Mol Biol Cell*

912   **24**:2861–75. doi:10.1091/mbc.E12-12-0857

913   Kovar DR, Harris ES, Mahaffy R, Higgs HN, Pollard TD. 2006. Control of the Assembly of

914   ATP- and ADP-Actin by Formins and Profilin. *Cell* **124**:423–435.

915   doi:10.1016/j.cell.2005.11.038

916   Kwiatkowski A V., Rubinson DA, Dent EW, Edward van Veen J, Leslie JD, Zhang J,

917   Mebane LM, Philippar U, Pinheiro EM, Burds AA, Bronson RT, Mori S, Fässler R,

918   Gertler FB. 2007. Ena/VASP Is Required for neuritogenesis in the developing cortex.

919   *Neuron* **56**:441–55. doi:10.1016/j.neuron.2007.09.008

37

920   Lai FPL, Szczodrak M, Block J, Faix J, Breitsprecher D, Mannherz HG, Stradal TE, Dunn

921   GA, Small JV, Rottner K. 2008. Arp2/3 complex interactions and actin network turnover

922   in lamellipodia. *EMBO J* **27**:982–92. doi:10.1038/emboj.2008.34

923   Lai FPL, Szczodrak M, Oelkers JM, Ladwein M, Acconcia F, Benesch S, Auinger S, Faix J,

924   Small JV, Polo S, Stradal TE, Rottner K. 2009. Cortactin promotes migration and

925   platelet-derived growth factor-induced actin reorganization by signaling to Rho-

926   GTPases. *Mol Biol Cell* **20**. doi:10.1091/mbc.E08-12-1180

927   Letort G, Ennomani H, Gressin L, Théry M, Blanchoin L. 2015. Dynamic reorganization of

928   the actin cytoskeleton. *F1000Research* **4**:940. doi:10.12688/f1000research.6374.1

929   Litschko C, Damiano-Guercio J, Brühmann S, Faix J. 2018. Analysis of Random Migration

930   of Dictyostelium Amoeba in Confined and Unconfined EnvironmentsMethods in

931   Molecular Biology (Clifton, N.J.). pp. 341–350. doi:10.1007/978-1-4939-7701-7_24

932   Loisel TP, Boujemaa R, Pantaloni D, Carlier M-F. 1999. Reconstitution of actin-based

933   motility of Listeria and Shigella using pure proteins. *Nature* **401**:613–616.

934   doi:10.1038/44183

935   Martiel J-L, Leal A, Kurzawa L, Balland M, Wang I, Vignaud T, Tseng Q, Théry M. 2015.

936   Measurement of cell traction forces with ImageJ. *Methods Cell Biol* **125**:269–87.

937   doi:10.1016/bs.mcb.2014.10.008

938   Mastronarde DN. 2005. Automated electron microscope tomography using robust prediction

939   of specimen movements. *J Struct Biol* **152**:36–51. doi:10.1016/j.jsb.2005.07.007

940   Mellor H. 2010. The role of formins in filopodia formation. *Biochim Biophys Acta* **1803**:191–

941   200. doi:10.1016/j.bbamcr.2008.12.018

942   Molinie N, Gautreau A. 2018. The Arp2/3 Regulatory System and Its Deregulation in Cancer.

943   *Physiol Rev* **98**:215–238. doi:10.1152/physrev.00006.2017

944   Mueller J, Szep G, Nemethova M, de Vries I, Lieber AD, Winkler C, Kruse K, Small JV,

945   Schmeiser C, Keren K, Hauschild R, Sixt M. 2017. Load Adaptation of Lamellipodial

946   Actin Networks. *Cell* **171**:188-200.e16. doi:10.1016/j.cell.2017.07.051

947   Mullins RD, Heuser JA, Pollard TD. 1998. The interaction of Arp2/3 complex with actin:

948   nucleation, high affinity pointed end capping, and formation of branching networks of

949   filaments. *Proc Natl Acad Sci U S A* **95**:6181–6. doi:10.1073/pnas.95.11.6181

950   Narita A, Mueller J, Urban E, Vinzenz M, Small JV, Maéda Y. 2012. Direct Determination of

951   Actin Polarity in the Cell. *J Mol Biol* **419**:359–368. doi:10.1016/j.jmb.2012.03.015

952   Nemethova M, Auinger S, Small JV. 2008. Building the actin cytoskeleton: filopodia

953   contribute to the construction of contractile bundles in the lamella. *J Cell Biol*

954   **180**:1233–1244. doi:10.1083/jcb.200709134

955   Olazabal IM, Caron E, May RC, Schilling K, Knecht DA, Machesky LM. 2002. Rho-kinase

956   and myosin-II control phagocytic cup formation during CR, but not FcgammaR,

957   phagocytosis. *Curr Biol* **12**:1413–18.

958   Oldenbourg R, Katoh K, Danuser G. 2000. Mechanism of Lateral Movement of Filopodia

959   and Radial Actin Bundles across Neuronal Growth Cones. *Biophys J* **78**:1176–1182.

960   doi:10.1016/S0006-3495(00)76675-6

961   Pellegrin S, Mellor H. 2005. The Rho Family GTPase Rif Induces Filopodia through mDia2.

962   *Curr Biol* **15**:129–133. doi:10.1016/j.cub.2005.01.011

963   Pollard TD. 2007. Regulation of Actin Filament Assembly by Arp2/3 Complex and Formins.

964   *Annu Rev Biophys Biomol Struct* **36**:451–477.

965   doi:10.1146/annurev.biophys.35.040405.101936

966   Pollard TD, Borisy GG. 2003. Cellular motility driven by assembly and disassembly of actin

967   filaments. *Cell* **112**:453–65.

968   Puleo JI, Parker SS, Roman MR, Watson AW, Eliato KR, Peng L, Saboda K, Roe DJ, Ros R,

969   Gertler FB, Mouneimne G. 2019. Mechanosensing during directed cell migration

970   requires dynamic actin polymerization at focal adhesions. *J Cell Biol*

971   **218**:jcb.201902101. doi:10.1083/jcb.201902101

972 Ran FA, Hsu PD, Wright J, Agarwala V, Scott DA, Zhang F. 2013. Genome engineering

973   using the CRISPR-Cas9 system. *Nat Protoc* **8**:2281–2308. doi:10.1038/nprot.2013.143

974 Reinhard M, Giehl K, Abel K, Haffner C, Jarchau T, Hoppe V, Jockusch BM, Walter U.

975   1995. The proline-rich focal adhesion and microfilament protein VASP is a ligand for

976   profilins. *EMBO J* **14**:1583–9.

977 Richter KN, Revelo NH, Seitz KJ, Helm MS, Sarkar D, Saleeb RS, D'Este E, Eberle J,

978   Wagner E, Vogl C, Lazaro DF, Richter F, Coy-Vergara J, Coceano G, Boyden ES,

979   Duncan RR, Hell SW, Lauterbach MA, Lehnart SE, Moser T, Outeiro TF, Rehling P,

980   Schwappach B, Testa I, Zapiec B, Rizzoli SO. 2018. Glyoxal as an alternative fixative to

981   formaldehyde in immunostaining and super-resolution microscopy. *EMBO J* **37**:139–

982   159. doi:10.15252/embj.201695709

983 Riedl J, Crevenna AH, Kessenbrock K, Yu JH, Neukirchen D, Bista M, Bradke F, Jenne D,

984   Holak TA, Werb Z, Sixt M, Wedlich-Soldner R. 2008. Lifeact: a versatile marker to

985   visualize F-actin. *Nat Methods* **5**:605–607. doi:10.1038/nmeth.1220

986 Rottner K, Behrendt B, Small J V, Wehland J. 1999. VASP dynamics during lamellipodia

987   protrusion. *Nat Cell Biol* **1**:321–2. doi:10.1038/13040

988 Rottner K, Faix J, Bogdan S, Linder S, Kerkhoff E. 2017. Actin assembly mechanisms at a

989   glance. *J Cell Sci* **130**. doi:10.1242/jcs.206433

990 Rottner K, Krause M, Gimona M, Small JV, Wehland J. 2001. Zyxin Is not Colocalized with

991   Vasodilator-stimulated Phosphoprotein (VASP) at Lamellipodial Tips and Exhibits

992   Different Dynamics to Vinculin, Paxillin, and VASP in Focal Adhesions. *Mol Biol Cell*

993   **12**:3103–3113. doi:10.1091/mbc.12.10.3103

994 Samarin S, Romero S, Kocks C, Didry D, Pantaloni D, Carlier M-F. 2003. How VASP

995   enhances actin-based motility. *J Cell Biol* **163**:131–142. doi:10.1083/jcb.200303191

996 Schaks M, Singh SP, Kage F, Thomason P, Klünemann T, Steffen A, Blankenfeldt W,

997   Stradal TE, Insall RH, Rottner K. 2018. Distinct Interaction Sites of Rac GTPase with

998   WAVE Regulatory Complex Have Non-redundant Functions in Vivo. *Curr Biol*

999   **28**:3674-3684.e6. doi:10.1016/j.cub.2018.10.002

1000 Scott JA, Shewan AM, den Elzen NR, Loureiro JJ, Gertler FB, Yap AS. 2006. Ena/VASP

1001   Proteins Can Regulate Distinct Modes of Actin Organization at Cadherin-adhesive

1002   Contacts. *Mol Biol Cell* **17**:1085–1095. doi:10.1091/mbc.e05-07-0644

1003 Skoble J, Auerbuch V, Goley ED, Welch MD, Portnoy DA. 2001. Pivotal role of VASP in

1004   Arp2/3 complex–mediated actin nucleation, actin branch-formation, and *Listeria*

1005   *monocytogenes* motility. *J Cell Biol* **155**:89–100. doi:10.1083/jcb.200106061

1006 Small J V. 1988. The actin cytoskeleton. *Electron Microsc Rev* **1**:155–74.

1007 Steffen A, Faix J, Resch GP, Linkner J, Wehland J, Small JV, Rottner K, Stradal TE. 2006.

1008   Filopodia formation in the absence of functional WAVE- and Arp2/3-complexes. *Mol*

1009   *Biol Cell* **17**. doi:10.1091/mbc.E05-11-1088

1010 Steffen A, Ladwein M, Dimchev GA, Hein A, Schwenkmezger L, Arens S, Ladwein KI,

1011   Holleboom JM, Schur F, Small JV, Schwarz J, Gerhard R, Faix J, Stradal TE,

1012   Brakebusch C, Rottner K. 2013. Rac function is crucial for cell migration but is not

1013   required for spreading and focal adhesion formation. *J Cell Sci* **126**:4572–4588.

1014   doi:10.1242/jcs.118232

1015 Steffen A, Rottner K, Ehinger J, Innocenti M, Scita G, Wehland J, Stradal TE. 2004. Sra-1

1016   and Nap1 link Rac to actin assembly driving lamellipodia formation. *EMBO J* **23**:749–

1017   59. doi:10.1038/sj.emboj.7600084

1018 Suraneni P, Rubinstein B, Unruh JR, Durnin M, Hanein D, Li R. 2012. The Arp2/3 complex

1019   is required for lamellipodia extension and directional fibroblast cell migration. *J Cell*

1020   *Biol* **197**:239–251. doi:10.1083/jcb.201112113

1021   Svitkina TM, Bulanova EA, Chaga OY, Vignjevic DM, Kojima S, Vasiliev JM, Borisy GG.

1022   2003. Mechanism of filopodia initiation by reorganization of a dendritic network. *J Cell*

1023   *Biol* **160**:409–421. doi:10.1083/jcb.200210174

1024   Urban E, Jacob S, Nemethova M, Resch GP, Small JV. 2010. Electron tomography reveals

1025   unbranched networks of actin filaments in lamellipodia. *Nat Cell Biol* **12**:429–435.

1026   doi:10.1038/ncb2044

1027   Vignaud T, Ennomani H, Théry M. 2014. Polyacrylamide Hydrogel MicropatterningMethods

1028   in Cell Biology. pp. 93–116. doi:10.1016/B978-0-12-417136-7.00006-9

1029   Vignjevic DM, Kojima S, Aratyn Y, Danciu O, Svitkina TM, Borisy GG. 2006. Role of

1030   fascin in filopodial protrusion. *J Cell Biol* **174**:863–875. doi:10.1083/jcb.200603013

1031   Vinzenz M, Nemethova M, Schur F, Mueller J, Narita A, Urban E, Winkler C, Schmeiser C,

1032   Koestler SA, Rottner K, Resch GP, Maeda Y, Small J V. 2012. Actin branching in the

1033   initiation and maintenance of lamellipodia. *J Cell Sci* **125**:2775–2785.

1034   doi:10.1242/jcs.107623

1035   Winkler C, Vinzenz M, Small JV, Schmeiser C. 2012. Actin filament tracking in electron

1036   tomograms of negatively stained lamellipodia using the localized radon transform. *J*

1037   *Struct Biol* **178**:19–28. doi:10.1016/j.jsb.2012.02.011

1038   Wu C, Asokan SB, Berginski ME, Haynes EM, Sharpless NE, Griffith JD, Gomez SM, Bear

1039   JE. 2012. Arp2/3 Is Critical for Lamellipodia and Response to Extracellular Matrix Cues

1040   but Is Dispensable for Chemotaxis. *Cell* **148**:973–987. doi:10.1016/j.cell.2011.12.034

1041   Yang C, Czech L, Gerboth S, Kojima S, Scita G, Svitkina T. 2007. Novel Roles of Formin

1042   mDia2 in Lamellipodia and Filopodia Formation in Motile Cells. *PLoS Biol* **5**:e317.

1043   doi:10.1371/journal.pbio.0050317

1044   Young LE, Heimsath EG, Higgs HN. 2015. Cell type-dependent mechanisms for formin-

1045   mediated assembly of filopodia. *Mol Biol Cell* **26**:4646–4659. doi:10.1091/mbc.E15-09-

1046   0626

1047   Young LE, Higgs HN. 2018. Focal Adhesions Undergo Longitudinal Splitting into Fixed-

1048   Width Units. *Curr Biol* **28**:2033-2045.e5. doi:10.1016/j.cub.2018.04.073

1049   Young LE, Latario CJ, Higgs HN. 2018. Roles for Ena/VASP proteins in FMNL3-mediated

1050   filopodial assembly. *J Cell Sci* **131**:jcs220814. doi:10.1242/jcs.220814

1051

1052
1053   **Figures**

1054   **Figure 1.** Loss of Ena/VASP-proteins impairs cell migration in B16-F1 cells. (**A**) To obtain

1055   independent triple-knockout mutant cell lines, the two independent Evl single knockout

1056   mutants (E-KO #23 and #27) derived from B16-F1 mouse melanoma cells, were separately

1057   used to the generate independent Evl/VASP double mutants (E/V-KO #23.7 and #27.9)

1058   followed by generation of two individual triple-KO mutants additionally lacking Mena

1059   (E/V/M-KO #23.7.66 and #27.9.12). Elimination of Evl, VASP and all Mena isoforms by

1060   CRISPR/Cas9 in B16-F1 cells was confirmed by immunoblotting using specific antibodies

1061   (asterisk indicates nonspecific band). GAPDH was used as loading control. (**B**) Consecutive

1062   gene disruption of the three Ena/VASP paralogues increasingly diminishes cell migration on

1063   laminin. At least three time-lapse movies from three independent experiments were analyzed

1064   for each cell line. (**C**) Directionality increased with consecutive inactivation of the three

1065   Ena/VASP paralogues. Bars represent arithmetic means ± SD. (**D**) Distribution of turning

1066   angles during migration of B16-F1 and derived mutant cells. (**E-G**) Cell speed and

1067   directionality are largely rescued by ectopic expression of EGFP-tagged VASP, Evl or Mena

1068   in EVM-KO #23 cells. (**F**) Bars represent arithmetic means ± SD. (**G**) Analyses of mean

1069   square displacement of wild-type *versus* mutant cells. Respective symbols and error bars

1070   represent means ± SEM. (B-E) The boxes in box plots indicate 50% (25-75%) and whiskers

43

1071 (5-95%) of all measurements, with dashed black lines depicting the medians, arithmetic

1072 means are highlighted in red. (B-C) and (E-F) Non-parametric, Kruskal-Wallis test and

1073 Dunn's Multiple Comparison test were used to reveal statistically significant differences

1074 between datasets. *p <0.05, **p <0.01, ***p <0.001; n.s.; not significant. n, number of cells

1075 analyzed from at least 3 independent experiments.

1076

1077 The following video and figure supplement are available for figure 1:

1078 **Figure 1-figure supplement 1**. Loss of Ena/VASP proteins affects migration and

1079 directionality. (**A**) Distribution of turning angles during migration of EVM-KO cells

1080 reconstituted with VASP, Evl or Mena. As opposed to Mena, VASP and Evl both readily

1081 rescued turning angles. (**B**) Analyses of mean square displacement of mutant and

1082 reconstituted cells. All three Ena/VASP members rescued migration as assessed by MSD, but

1083 VASP was most efficient. Respective symbols and error bars represent means ± SEM.

1084

1085 **Figure 1-video 1**. Loss of Ena/VASP proteins in B16-F1 cells impairs cell migration, related

1086 to *Figure 1*. Random migration of B16-F1, and derived Evl-KO (E-KO), Evl/VASP-KO

1087 (EV-KO) and Evl/VASP/Mena-KO (EVM-KO) mutants on laminin. Cells were recorded by

1088 phase-contrast time-lapse imaging using a 4x objective and tracked by MTrackJ to illustrate

1089 representative cell trajectories. Note more directional movement of EVM-KO cells. Time is

1090 indicated in h:min. Bar, 300 µm.

1091

1092 **Figure 2.** Inactivation of Ena/VASP proteins in various fibroblasts impairs cell migration.

1093 (**A**) MV^{D7} cells lack Mena and VASP, but still express Evl. Elimination of Evl by

1094 CRISPR/Cas9 in MV^{D7} fibroblasts was confirmed by immunoblotting in independent clonal

1095 cell lines (MVE-KO). GAPDH was used as loading control. Asterisk indicates nonspecific

1096   band in Mena blot. (**B**) Elimination of Evl in MV^{D7} cells decreased cell speed on fibronectin-

1097   coated glass and could be rescued by expression of Evl. (**C**) Analyses of mean square

1098   displacement of MV^{D7}, MVE-KO and reconstituted cells as indicated. Data points represent

1099   arithmetic means ± SEM. At least three time-lapse movies from three independent

1100   experiments were analyzed for each cell line. (**D**) Representative frames from wound healing

1101   movies of MV^{D7}, MVE-KO and reconstituted cells as indicated. MVE-KO cells were not able

1102   to close the wound after 17 hours. Bar, 200 μm. (**E**) Reduction of wound area over time. n,

1103   number of movies analyzed. Data are means ± SD. (**F**) Average wound closure rate. n,

1104   number of movies analyzed. (**G**) Immunoblot of independent single and double-KO mutants

1105   derived from NIH 3T3 fibroblasts lacking Mena (M-KO) or Mena and VASP (MV-KO) by

1106   CRISPR/Cas9 technology. GAPDH was used as loading control. (**H**) Consistent with

1107   findings in B16-F1 cells, consecutive gene disruption of these two Ena/VASP paralogues in

1108   NIH 3T3 fibroblasts again increasingly diminished cell migration on fibronectin. (**I**) Analyses

1109   of mean square displacement of NIH 3T3, M-KO and MV-KO cells as indicated. Data points

1110   represent arithmetic means ± SEM. n, number of cells tracked. At least three time-lapse

1111   movies from three independent experiments were analyzed for each cell line. (**J**) Total

1112   cytoplasmic concentrations of Ena/VASP proteins in investigated cell lines. (B, F and H)

1113   Boxes in box plots indicate 50% (25-75%) and whiskers (5-95%) of all measurements, with

1114   dashed black lines depicting the medians, arithmetic means are highlighted in red. Non-

1115   parametric, Kruskal-Wallis test and Dunn's Multiple Comparison test were used to reveal

1116   statistically significant differences between datasets. *p <0.05, **p <0.01, ***p <0.001; n.s.;

1117   not significant. n, number of cells analyzed from at least 3 independent experiments.

1118

1119   The following figure supplement is available for figure 2:

1120 **Figure 2-figure supplement 1.** Elimination of Evl in MV^{D7} cells affects directionality. (**A**)

1121 Quantification of directionality. Bars represent arithmetic means ± SD. ***p<0.001 and n.s.,

1122 not significant by Kruskal-Wallis test and Dunn's Multiple Comparison test and n, number of

1123 cells analyzed. (**B**) Radar plots showing trajectories of 15 randomly migrating MV^{D7}, MVE-

1124 KO and reconstituted cells as indicated. Note higher directional persistence of MVE-KO cells

1125 compared to MV^{D7} cells, which was diminished again by expression of Evl. Scale bar, 100

1126 μm.

1127

1128 **Figure 3.** Loss of Ena/VASP perturbs lamellipodia and abrogates microspike formation in

1129 B16-F1 cells. (**A**) Representative examples of lamellipodia from wild-type B16-F1, EVM-

1130 KO and reconstituted EVM-KO cells transiently expressing EGFP-VASP. Cells migrating on

1131 laminin and stained for the actin cytoskeleton with phalloidin. Bar, 10 μm. (**B**) Quantification

1132 of F-actin intensities in lamellipodia (red circle in A) of wild-type and mutant cells after

1133 subtraction of background (blue circle in A). (**C**) Quantification of lamellipodia width in

1134 wild-type and mutant cells. (**D**) Loss of Ena/VASP markedly diminishes fascin-decorated

1135 microspikes, which are rescued by EGFP-VASP. Immunostaining with fascin antibody. Bar,

1136 10 μm. (**E**) Quantification of microspikes in wild-type and mutant cells. (**F**) Quantification of

1137 microspike length in wild-type and mutant cells. (**G**) Comparable expression of fascin in

1138 wild-type and EVM-KO cells was confirmed by immunoblotting using fascin-specific

1139 antibodies. GAPDH was used as loading control. (**H**) Representative examples of

1140 lamellipodia from wild-type B16-F1 cells, single E-KO, double EV-KO and triple EVM-KO

1141 mutants. Displayed cells migrating on laminin were fixed and stained with phalloidin to

1142 visualize their F-actin cytoskeleton. Bars, 10 μm. Note presence of microspikes in B16-F1

1143 wild-type cells, single E-KO and double EV-KO mutants, but not in the triple EVM-KO

1144 mutant cell. (**B**-C and E-**F**) Boxes in box plots indicate 50% (25-75%) and whiskers (5-95%)

1145   of all measurements, with dashed black lines depicting the medians, arithmetic means are

1146   highlighted in red. Non-parametric, Kruskal-Wallis test and Dunn's Multiple Comparison test

1147   were used to reveal statistically significant differences between datasets. ***$p < 0.001$; n.s.;

1148   not significant. n, number of cells analyzed (B, C, and E) or microspikes (F) from at least 3

1149   independent experiments.

1150

1151   The following video and figure supplement are available for figure 3:

1152   **Figure 3-figure supplement 1.** Expression of Evl and Mena is sufficient for rescuing of

1153   lamellipodia in B16-F1 cells. **(A)** Representative examples of lamellipodia in wild-type B16-

1154   F1, EVM-KO and reconstituted EVM-KO cells transiently expressing EGFP-Evl or -Mena,

1155   as indicated. Cells migrating on laminin were fixed and stained with phalloidin to visualize

1156   the actin cytoskeleton. Bar, 10 μm. (**B**) Quantification of F-actin intensities in lamellipodia of

1157   wild-type, mutant and reconstituted cells after background subtraction. (**C**) Quantification of

1158   lamellipodia widths in cells indicated. (B-C) Boxes in box plots indicate 50% (25-75%) and

1159   whiskers (5-95%) of all measurements, with dashed black lines depicting the medians,

1160   arithmetic means are highlighted in red. Non-parametric, Kruskal-Wallis test and Dunn's

1161   Multiple Comparison test were used to reveal statistically significant differences between

1162   datasets. *$p < 0.05$, **$p < 0.01$, ***$p < 0.001$; n.s.; not significant. n, number of cells analyzed

1163   from at least 3 independent experiments.

1164

1165   **Figure 3-video 1**. Elimination of all three Ena/VASP proteins impairs lamellipodium

1166   formation and abolishes microspikes, related to *Figure 3*. Displayed cells were transfected

1167   with EGFP-LifeAct to monitor actin dynamics during migration on laminin by time-lapse

1168   imaging using a 40x objective. EVM-KO cells were additionally transfected with mCherry-

1169 VASP (not shown). Reconstitution of EVM-KO cells with mCherry-VASP restored

1170 lamellipodium and microspike formation. Time is indicated in min:s. Bar, 15 µm.

1171

1172 **Figure 3-video 2**. Elimination of all three Ena/VASP proteins abrogates microspikes, related

1173 to *Figure 3*. The cells shown were transfected with EGFP-fascin to monitor microspikes in

1174 cells migrating on laminin by time-lapse imaging using a 40x objective. EVM-KO cells were

1175 additionally transfected with mCherry-VASP (not shown). Reconstitution of EVM-KO cells

1176 with mCherry-VASP fully restored microspike formation (right panel). Time is indicated in

1177 min:s. Bar, 15 µm.

1178

1179 **Figure 4.** Microspike formation is exclusively rescued by all three Ena/VASP members, but

1180 not by active Rif-L77, myosin X, active mDia2ΔDAD or active FMNL2 and -3. (**A**) Images

1181 display cells stained for the actin cytoskeleton with phalloidin and respective, expressed

1182 EGFP-tagged protein as indicated. Bars, 20 µm. (**B**) EVM-KO cells form filopodia in the

1183 absence of lamellipodia. Representative examples of phalloidin-stained wild-type B16-F1 and

1184 EVM-KO cells devoid of lamellipodia after treatment with 200 µM CK666 seeded at low

1185 laminin (1µg/mL). Bar, 10 µm. (**C**) Quantification of filopodia in CK666-treated B16-F1 and

1186 EVM-KO cells. (**D**) Unchanged filopodium formation in B16-F1 and EVM-KO cells

1187 triggered by transient expression of active mDia2. Representative examples of B16-F1 and

1188 EVM-KO cells after labelling with GFP nanobodies are shown. Bar, 10 µm. (**E**)

1189 Quantification of filopodia revealed no difference between wild-type and mutant cells. (C and

1190 E) Boxes in box plots indicate 50% (25-75%) and whiskers (5-95%) of all measurements,

1191 with dashed black lines depicting the medians, arithmetic means are highlighted in red. Non-

1192 parametric, by Mann-Whitney U rank sum test was used to reveal statistically significant

48

1193   differences between datasets. ***p <0.001; n.s.; not significant. n, number of cells analyzed

1194   from at least 3 independent experiments.

1195

1196   The following figure supplement is available for figure 4:

1197   **Figure 4-figure supplement 1.** Quantification of microspikes after rescue of EVM-KO cells

1198   with EGFP-tagged Evl or Mena. (**A**) Quantification of microspikes per cell. (**B**)

1199   Quantification of microspike length. Note longer microspikes in reconstituted EVM-KO cells

1200   expressing Mena. (A-B) **p<0.01, ***p<0.001; n.s. not significant by Kruskal-Wallis test

1201   and Dunn's Multiple Comparison test. n, number of cells analyzed.

1202

1203   **Figure 5.** Loss of Ena/VASP affects lamellipodial parameters and protrusion dynamics. (**A**)

1204   Immunolabelling of the Arp2/3 complex subunit p16-ARC (ArpC5A) in wild-type, mutant

1205   and reconstituted cells as indicated. Bar, 10 μm. (**B**) Quantification of Arp2/3 complex

1206   intensities in lamellipodia. (**C**) Quantification of Arp2/3 complex signal width. (**D**)

1207   Immunolabelling of CP in cell types as indicated. Bar, 10 μm. (**E**) Quantification of CP

1208   signal intensities in lamellipodia. (**F**) Quantification of CP signal width in lamellipodia. (**G**)

1209   Loss of Ena/VASP reduces the efficiency of lamellipodium protrusion. Kymographs of

1210   representative phase-contrast movies are shown. Bar, 10 μm. (**H**) Multiple examples of

1211   lamellipodium protrusion in B16-F1 *versus* EVM-KO *versus* EVM-KO cells reconstituted

1212   with VASP. (**I**) Quantification of protrusion rates. B-C, E-F and I, *p<0.05, ***p<0.001 and

1213   n.s., not significant by Kruskal-Wallis test and Dunn's Multiple Comparison test. n, number

1214   of cells. (**J**) Quantification of protrusion persistence. (**K**) FRAP of EGFP-ß-actin in

1215   lamellipodia of B16-F1 and EVM-KO cells bleached as indicated by white rectangles.

1216   Numbers in post-bleach images correspond to seconds after bleach. Bar, 3 μm. (**L**) Average

1217   actin assembly rates of respective cell types expressing EGFP-ß-actin. Note reduced

49

1218   lamellipodial actin assembly in the mutant. J-L, ***p <0.001, n.s., not significant by Mann-

1219   Whitney U rank sum test. n, number of cells analyzed.

1220

1221   The following video and figure supplement are available for figure 5:

1222   **Figure 5-figure supplement 1.** Loss of Ena/VASP affects additional lamellipodial

1223   parameters. (**A**) Immunolabelling of endogenous Arp2/3 complex subunit p16-ARC

1224   (ArpC5A) in B16-F1 wild-type, EVM-KO and reconstituted EVM-KO cells expressing Evl

1225   or Mena. Bar, 10 µm. (**B**) Quantification of p16-ARC intensities in lamellipodia. (**C**)

1226   Quantification of p16-ARC width. (**D**) Immunolabelling of endogenous CP in wild-type,

1227   mutant and reconstituted cells. Bar, 10 µm. (**E**) Quantification of CP intensities in

1228   lamellipodia. (**F**) Quantification of CP width in lamellipodia. (**G**) Immunolabelling of

1229   endogenous cortactin in wild-type, mutant and reconstituted cells. Bar, 10 µm. (**H**)

1230   Quantification of cortactin intensities in lamellipodia. (**I**) Quantification of cortactin width in

1231   lamellipodia. B-C, E-F and H-I, * p< 0.05, **p<0.01, ***p<0.001, n.s., not significant by

1232   Kruskal-Wallis test and Dunn's Multiple Comparison test. n, number of cells analyzed. (**J-K**)

1233   Immunolabelling of endogenous WAVE2 revealed no differences between B16-F1 wild-type

1234   and EVM-KO cells. Bar, 10 µm. n.s., not significant by Mann-Whitney U rank sum test. n,

1235   number of analyzed cells. (**L**) Comparable amounts of expression of WAVE2 in wild-type

1236   and EVM-KO cells were confirmed by immunoblotting using WAVE2-specific antibodies.

1237   GAPDH was used as loading control.

1238   **Figure 5-video 1**. Impaired protrusion of EVM-KO cells migrating on laminin, related to

1239   *Figure 5*. Reconstitution of the triple mutant cells with EGFP-VASP fully restored

1240   lamellipodial protrusion. Cells were recorded by time-lapse phase-contrast imaging using a

1241   40x objective. Time is indicated in min:s. Bar, 15 µm.

1242

50

1243   **Figure 5-video 2**. Loss of Ena/VASP in B16-F1 cells reduces actin network polymerization,

1244   related to *Figure 5*. Representative time-lapse movies showing FRAP experiments on

1245   lamellipodia of B16-F1 wild-type or EVM-KO cells, as indicated, expressing EGFP-β-actin

1246   on laminin. Time-lapse movies show periods before and after bleaching of lamellipodial

1247   regions with bleaching time points set to 0 sec in each case. Bar, 3 μm.

1248

1249   **Figure 6.** Electron tomography of ultrastructural changes in lamellipodial actin networks. (**A**)

1250   Transmission electron micrographs of representative wild-type (B16-F1) and EVM-KO cells

1251   showing distinct actin filament networks at the leading edge (left), and 2D projections of

1252   digital 3D tomograms showing either actin filament trajectories in green (middle), or barbed

1253   ends on grey filaments in red, and pointed ends in blue (right). Scale bar, 100 nm. (**B**)

1254   Quantification of filament length in wild-type and EVM-KO cells. ***p <0.001 by Mann-

1255   Whitney U rank sum test. Whiskers indicate 10% and 90% confidence intervals. n indicates

1256   the number of filaments analyzed. Dashed black lines show median, red lines arithmetic

1257   mean. (**C**) Densities of filaments, barbed and pointed ends in 106 nm-wide spatial bins

1258   throughout the lamellipodium. Error bars indicate SEM. 6 tomograms for each cell line were

1259   analyzed. (**D**) Histogram showing frequencies of filament angles to the leading edge (90°

1260   corresponding to filaments perpendicular to the leading edge). Dashed black lines are

1261   medians, and red lines arithmetic means.

1262

1263   The following video is available for figure 6:

1264   **Figure 6-video 1**. Loss of Ena/VASP deteriorates lamellipodium architecture in B16-F1

1265   cells, related to *Figure 6*. Animated visualization of the three-dimensional organization of

1266   lamellipodia of B16-F1 wild-type and EVM-KO cells resolved by electron tomography. A

1267   3D model of the actin filament network corresponds to Figure 6A and was obtained by

1268   automatic tracking of filaments through the tomogram slices.

1269

1270   **Figure 7.** Inactivation of Evl in MV^{D7} cells impairs FA formation. (**A**) Spreading of MV^{D7},

1271   EVM-KO and reconstituted cells on fibronectin. EGFP-Evl expressing cell are marked by red

1272   asterisks. Time is in minutes. Bar, 25 μm. (**B**) Quantification of cell area over time. Data are

1273   means ± SEM. n, number of analyzed cells from 5 independent experiments. (**C**)

1274   Quantification of spreading rate. (**D**) Expression of EGFP-tagged Evl, -VASP or -Mena in

1275   MVE-KO cells promotes the formation of FA. Immunolabeling of EGFP and vinculin in cells

1276   seeded on fibronectin. Bars, 20 μm. (**E**) Representative micrographs of MV^{D7}, MVE-KO and

1277   reconstituted cells displaying vinculin staining before *(upper panel)* and after processing by

1278   Focal Adhesion Analysis Server (*lower panel*). Bar, 10 μm. (**F**) Quantification of vinculin

1279   intensities in FA. (**G**) Quantification of FA size. (**H**) Quantification of FA number per cell. (C

1280   and H) $*p<0.05$, $**p<0.01$, $***p<0.001$ and n.s., not significant by Kruskal-Wallis test and

1281   Dunn's Multiple Comparison test or by one-way ANOVA and Tukey Multiple Comparison

1282   test (F-G), respectively. n, number of analyzed cells from 3 independent experiments. Boxes

1283   in box plots indicate 50% (25-75%) and whiskers (5-95%) of all measurements, with dashed

1284   black lines depicting the medians, arithmetic means are highlighted in red.

1285

1286   The following video and figure supplement are available for figure 7:

1287   **Figure 7-figure supplement 1.** Loss of Ena/VASP proteins affects cell spreading and FA

1288   formation in B16-F1 cells. (**A**) Spreading of B16-F1, EVM-KO and reconstituted cells on

1289   laminin-coated glass. EGFP-VASP or EGFP-Evl expressing EVM-KO cells are marked by

1290   red asterisks. Time is in minutes. Scale bar, 25 μm. (**B**) Quantification of cell area over time.

1291   Bars and error bars represent arithmetic means and SEM, respectively. n, number of analyzed

1292   cells from 5 independent experiments. (**C**) Quantification of spreading rate. *p<0.05,

1293   **p<0.01, ***p<0.001 and n.s., not significant by Kruskal-Wallis test and Dunn's Multiple

1294   Comparison test. n, number of analyzed cells from at least 3 independent experiments.

1295

1296   **Figure 7-video 1**. Loss of Evl in MV^{D7} cells diminishes spreading on fibronectin, related to

1297   *Figure 7*. MV^{D7}, MVE-KO and reconstituted cells expressing EGFP-Evl were seeded onto

1298   fibronectin and recorded by time-lapse phase-contrast imaging using a 20x objective.

1299   Reconstituted cells are highlighted by asterisks. Note enhanced spreading in MVE-KO cells

1300   expressing EGFP-Evl. Time, min:s. Scale bar, 25 μm.

1301

1302   **Figure 8.** Confined MVE-KO cells exhibit diminished traction forces. (**A**) Representative

1303   micrographs of cells plated on crossbow-shaped polyacrylamide micropatterns coated with

1304   fibronectin. MV^{D7} and MVE-KO were stained with CellTracker^{TM} Green and rescued cells

1305   were stably expressing EGFP-Evl. Bar, 10 μm. (**B** and **D**) Quantifications of contractile

1306   energy of MV^{D7}, MVE-KO and Evl expressing cells plated on crossbow-shaped

1307   polyacrylamide micropatterns in independent experiments. ***p<0.001 by Mann-Whitney U

1308   rank sum test. n, number of cells analyzed. Boxes in box plots indicate 50% (25-75%) and

1309   whiskers (5-95%) of all measurements, with dashed black lines depicting the medians,

1310   arithmetic means are highlighted in red. (**C** and **E**) Images depicting averaged traction force

1311   field representations of cells indicated. Bar, 10 μm. Force scale bar is in Pascal and arrows

1312   represent the local force magnitude and orientation.

1313

1314   The following figure supplement is available for figure 8:

1315   **Figure 8-figure supplement 1.** Inactivation of Evl in unconfined MV^{D7} cells diminishes cell

1316   contractile energy. (**A**) Quantifications of contractile energy normalized by cellular area and

1317   measured for MV^{D7}, MVE-KO and Evl-rescue of MVE-KO cells plated on plain

1318   polyacrylamide micropatterns coated with fibronectin. ***p<0.001 or n.s., not significant by

1319   Kruskal-Wallis test and Dunn's Multiple Comparison test. n, number of cells analyzed.

1320   Boxes in box plots indicate 50% (25-75%) and whiskers (5-95%) of all measurements, with

1321   dashed black lines depicting the medians, arithmetic means are highlighted in red. (**B**) Images

1322   depicting representative traction force field representations from cells of distinct genotypes,

1323   as indicated. Force scale bar is in Pascal and arrows represent local force magnitude and

1324   orientation.
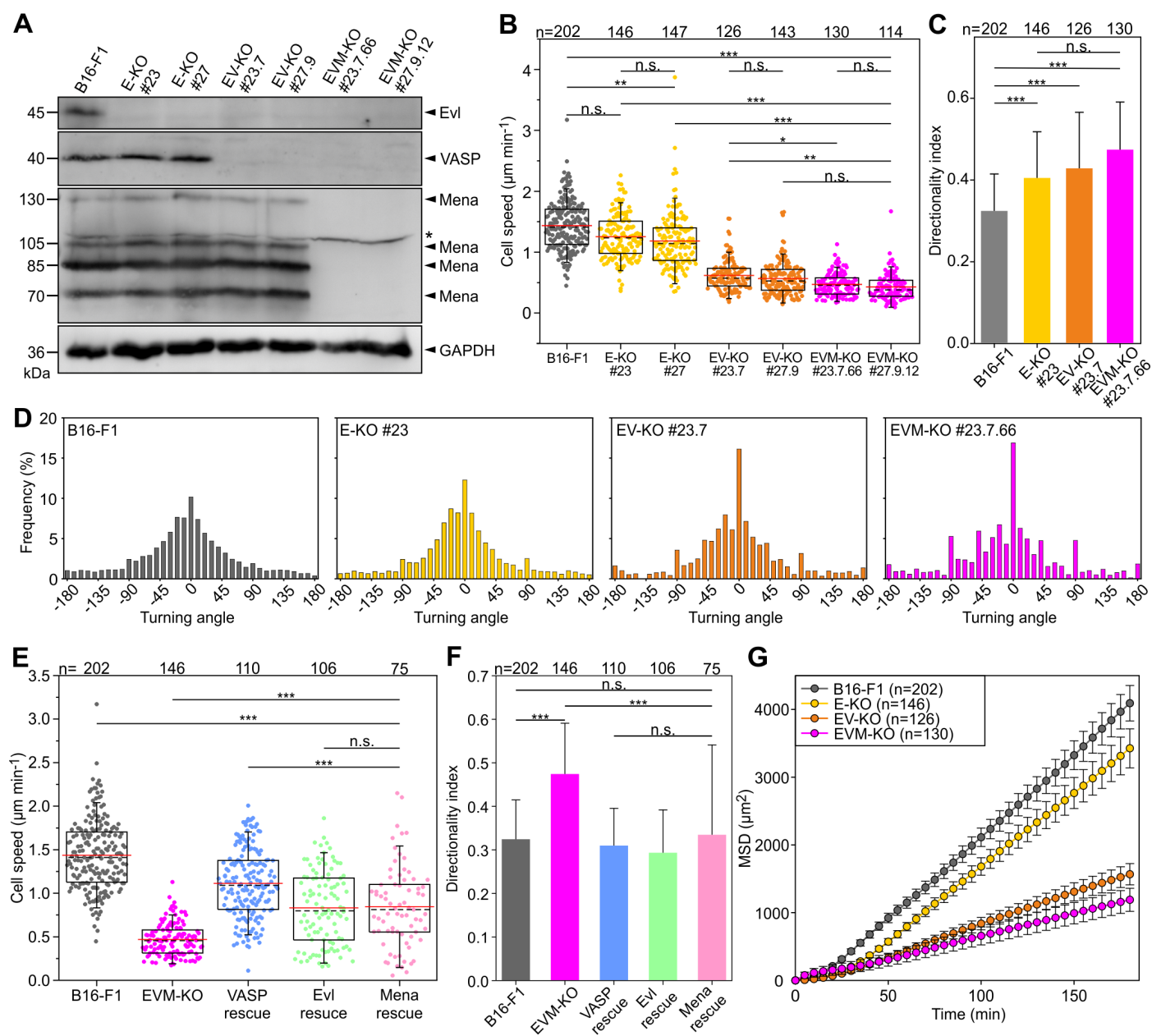
Figure 1

Figure 2

Figure 3

A EVM-KO

B 200 μM CK666

C

D

E
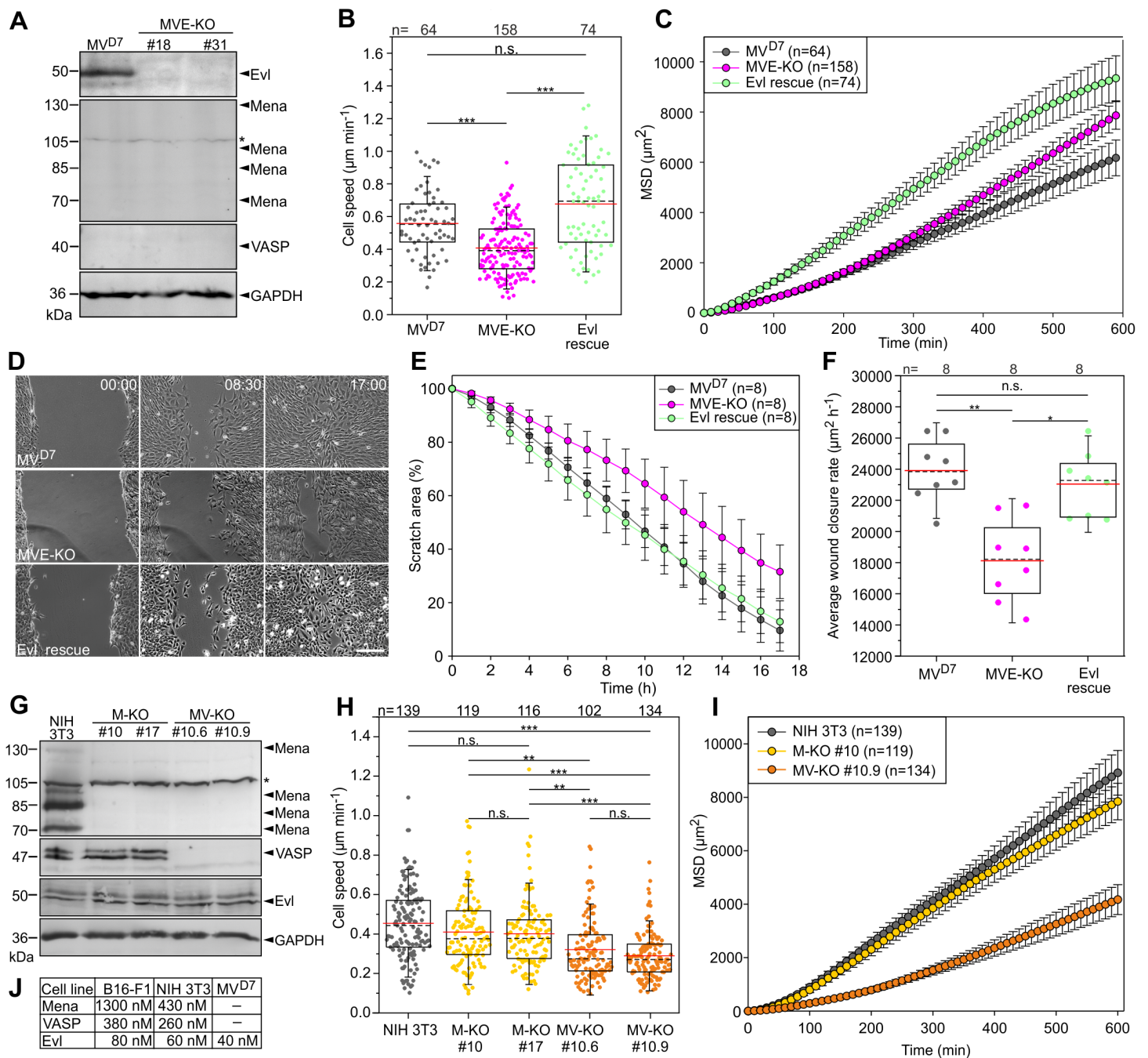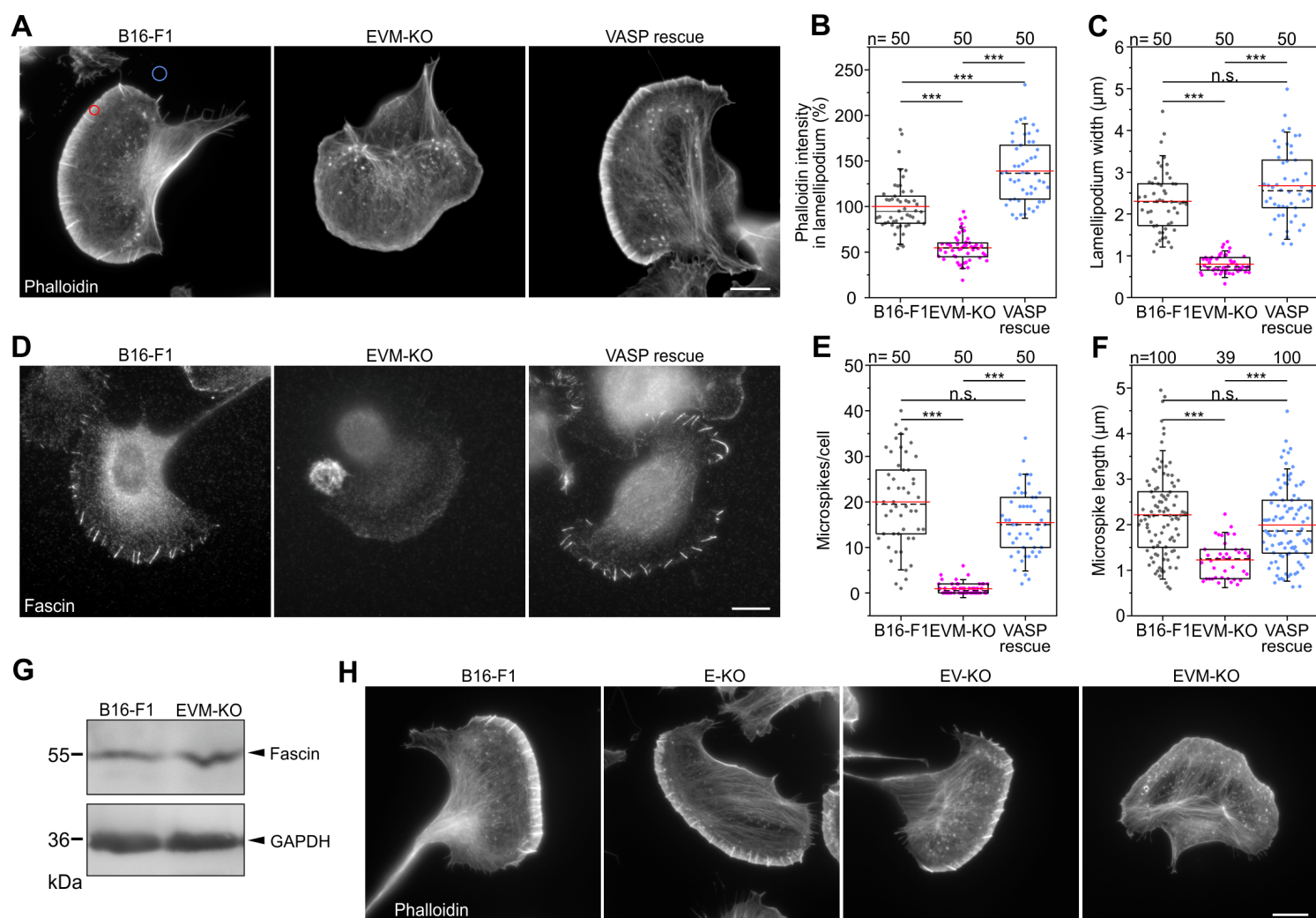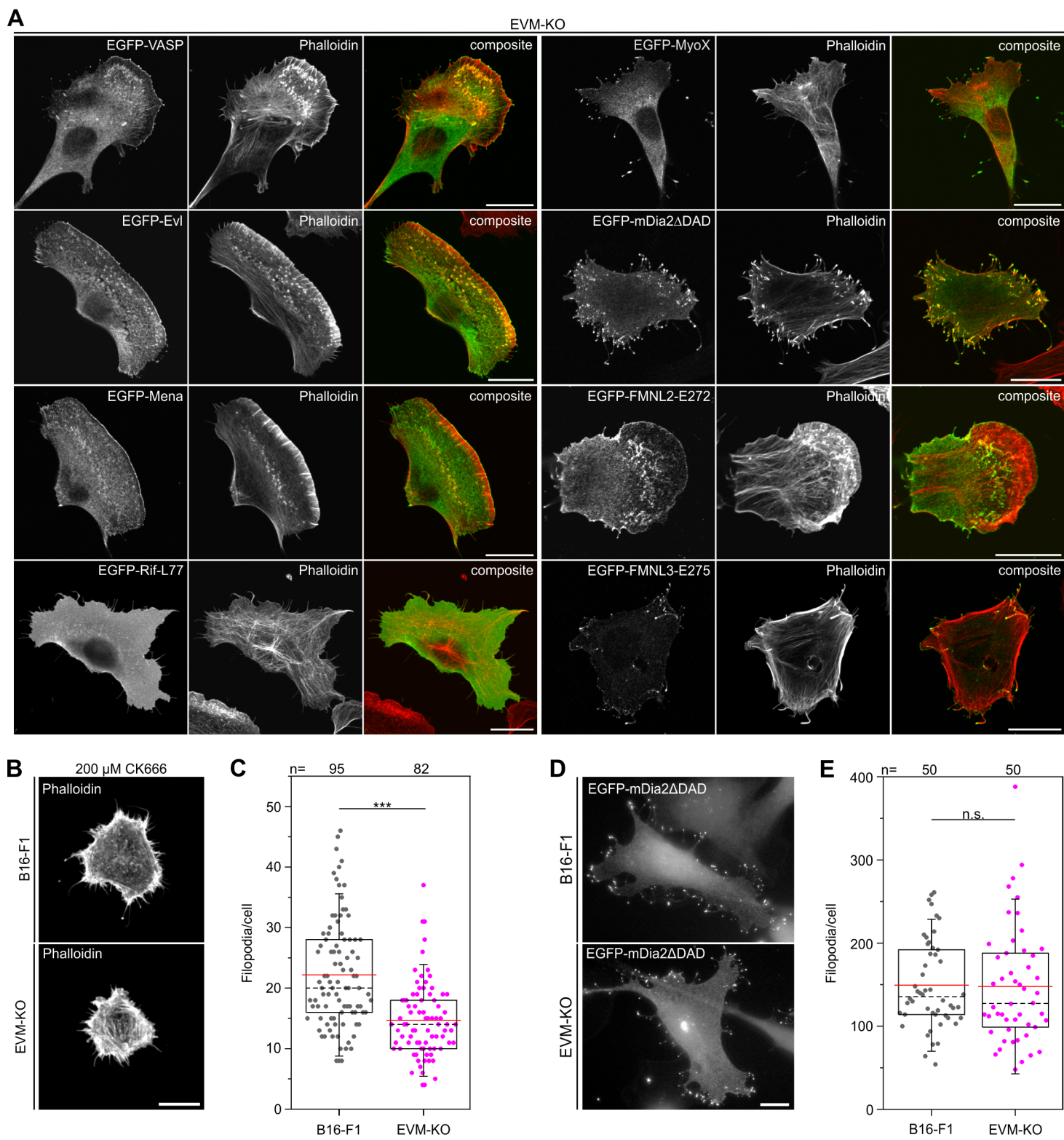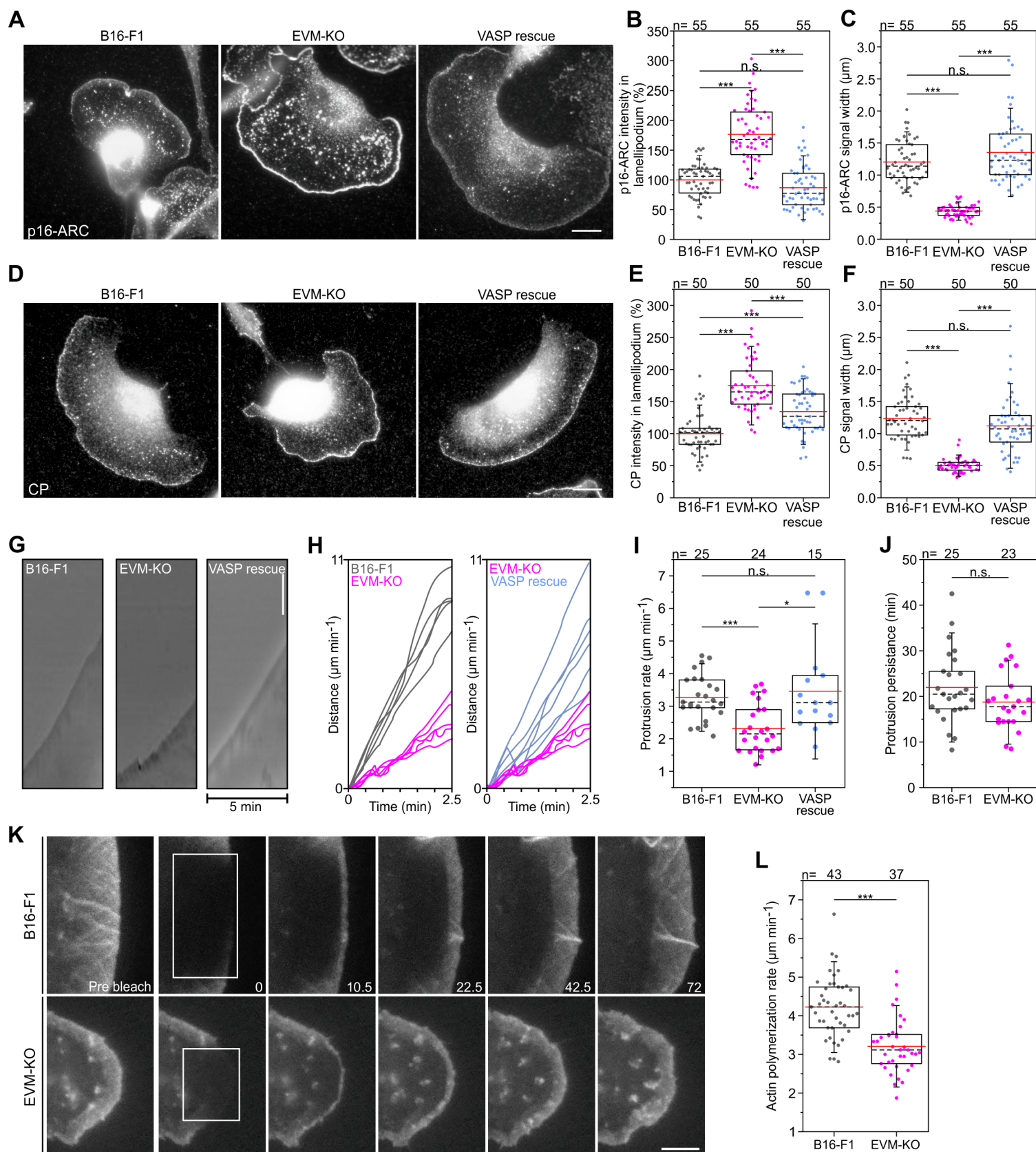
Figure 4

Figure 5

Figure 6

Figure 7

A micropattern   MV^{D7} MVE-KO   MVE-KO Evl-rescue

ECM-Alexa647   CellTracker   EGFP
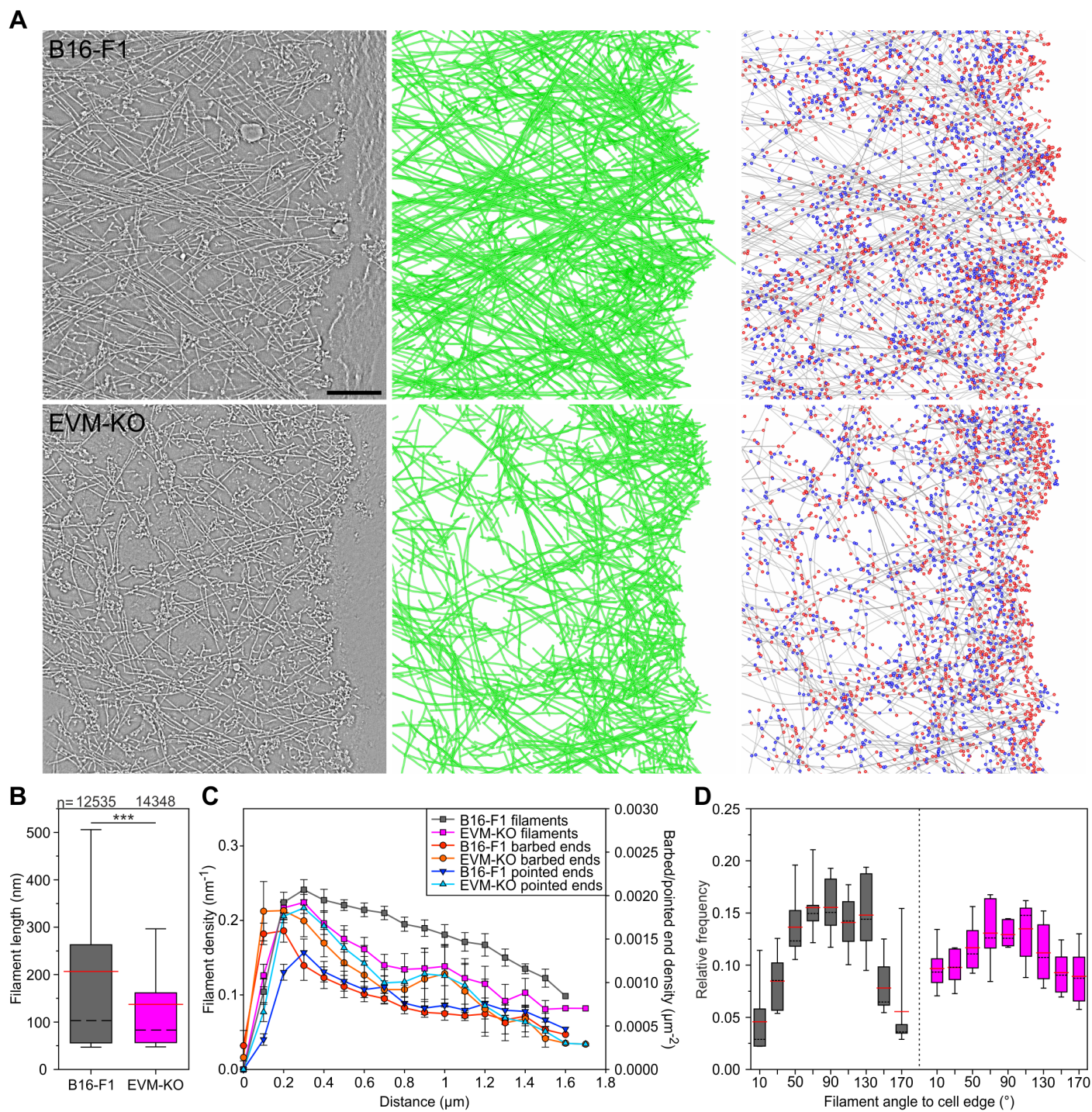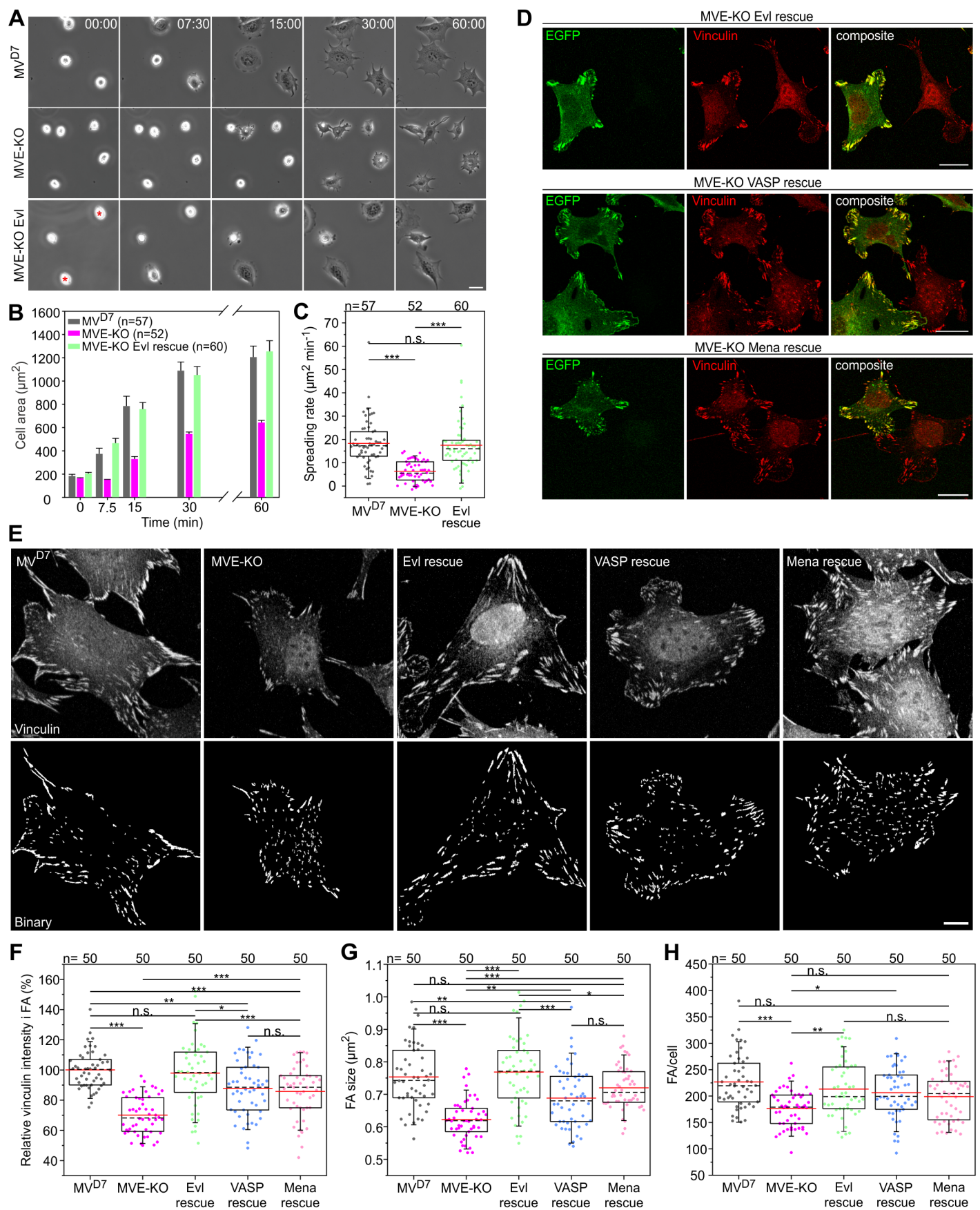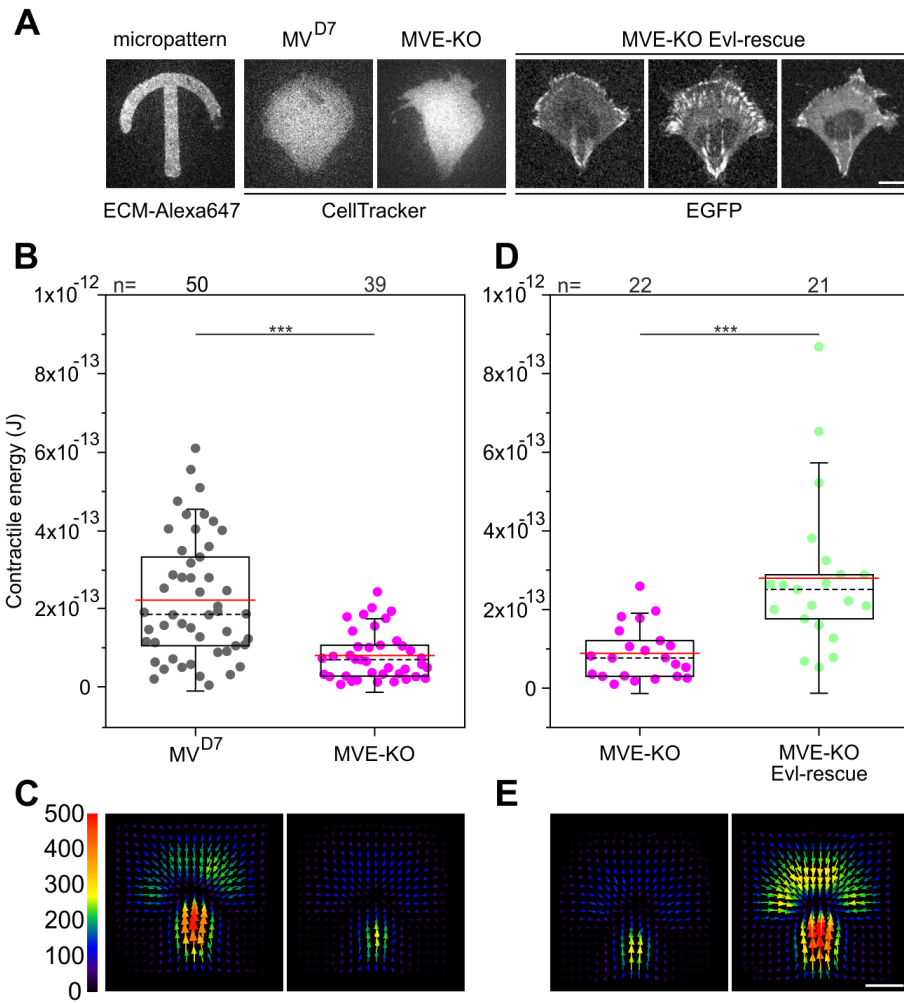
Figure 8

Figure 1-figure supplement 1
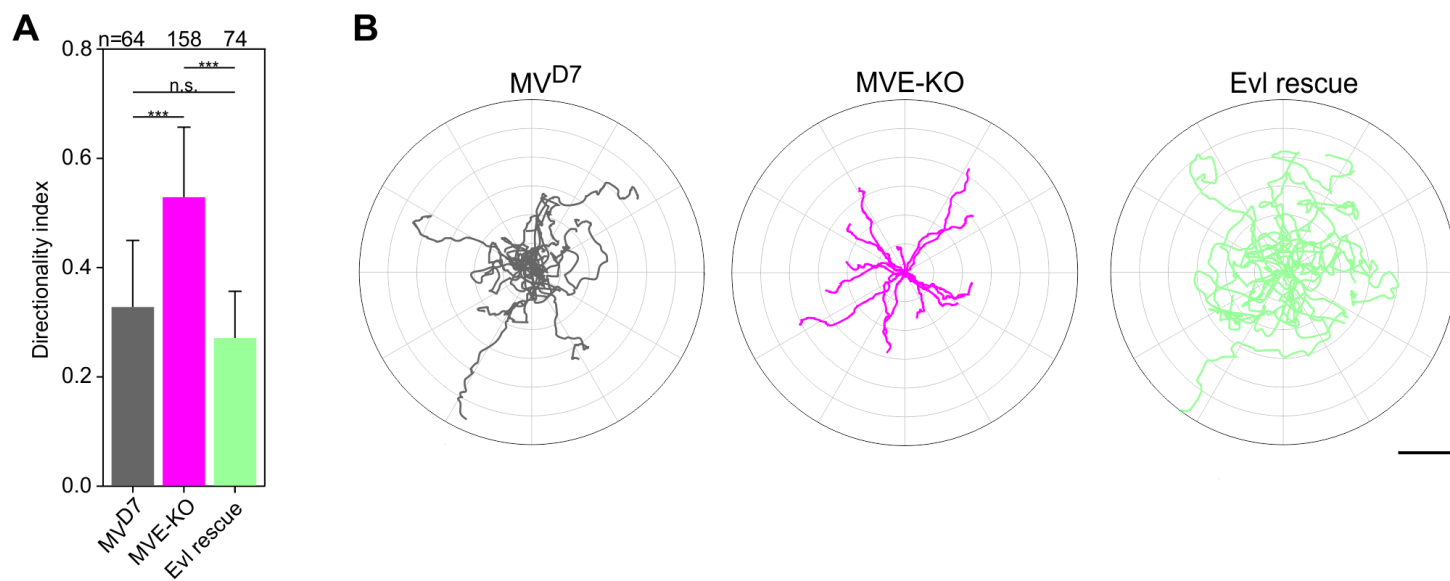
A

B

MV^{D7}   MVE-KO   Evl rescue
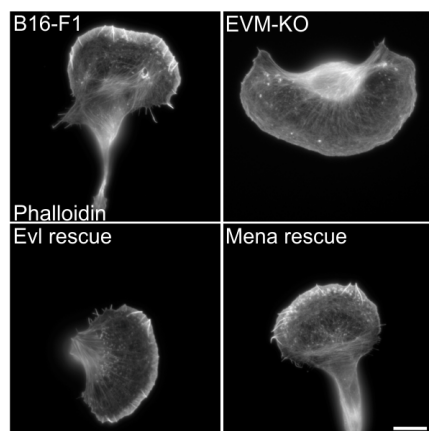

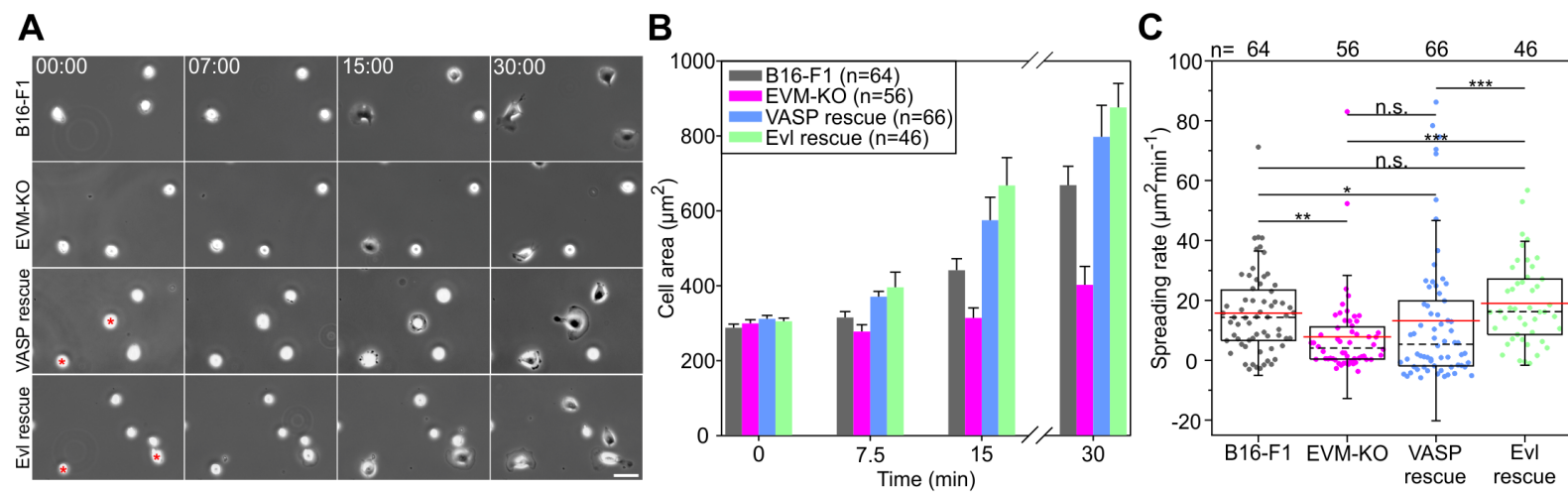Figure 2-figure supplement 1

Figure 3-figure supplement 1

A

n= 50   50   50   50

Microspikes/ cell

**   ***

***

n.s.

B16-F1   EVM-KO   Evl rescue   Mena rescue

B

n=100   27   100   100

Microspike length (µm)

***

n.s.

**

***

B16-F1   EVM-KO   Evl rescue   Mena rescue
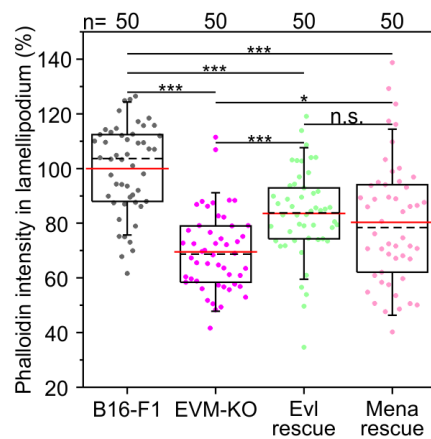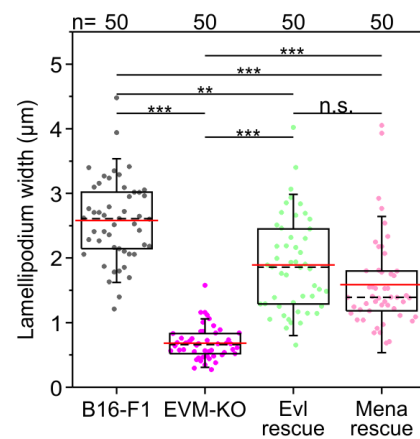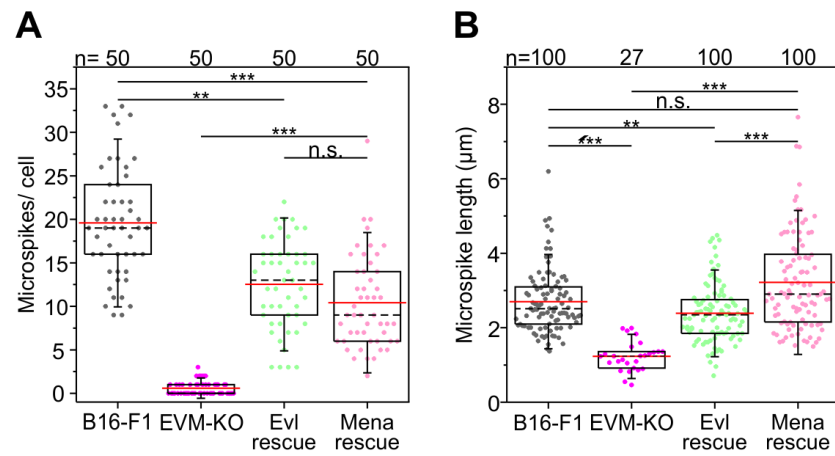
Figure 4-figure supplement 1
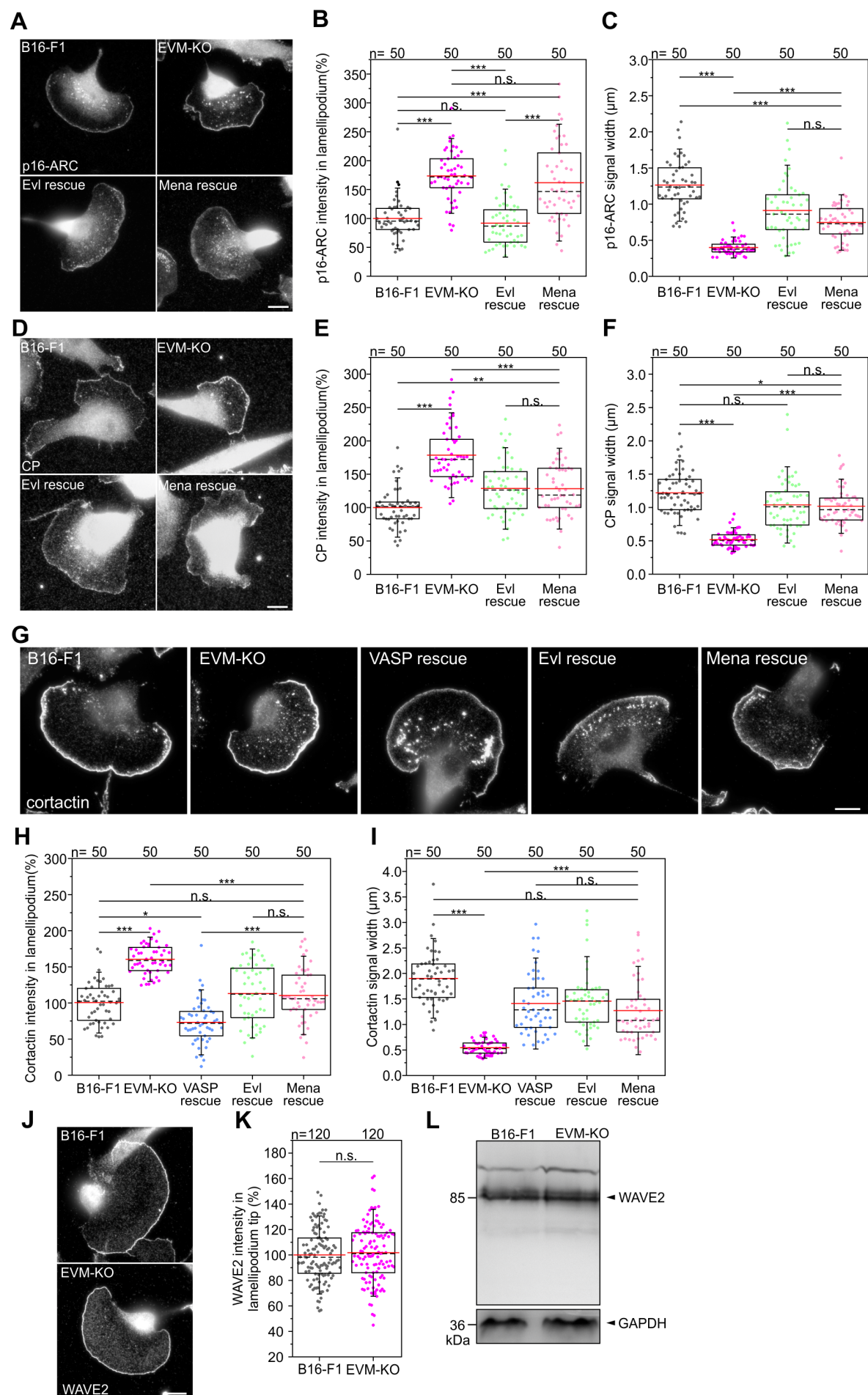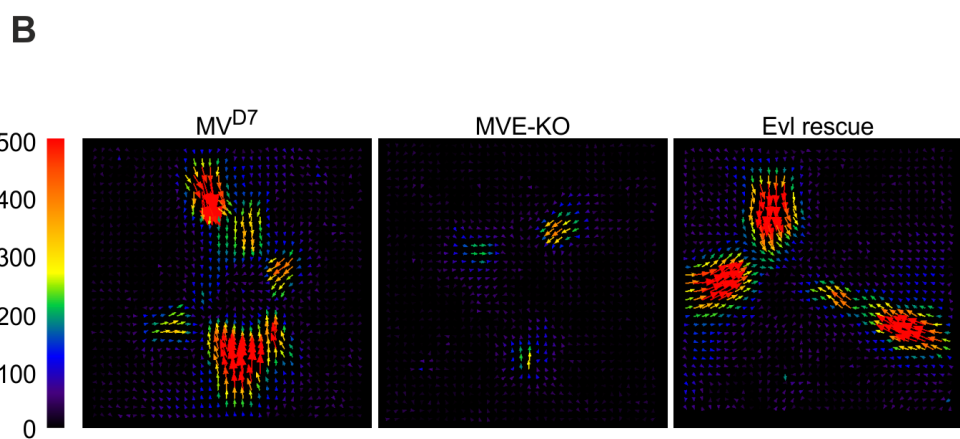
Figure 5-figure supplement 1

Figure 7-figure supplement 1

A

Contractile energy/area (J.μm⁻²)

n= 20   17   25

n.s.

***

***

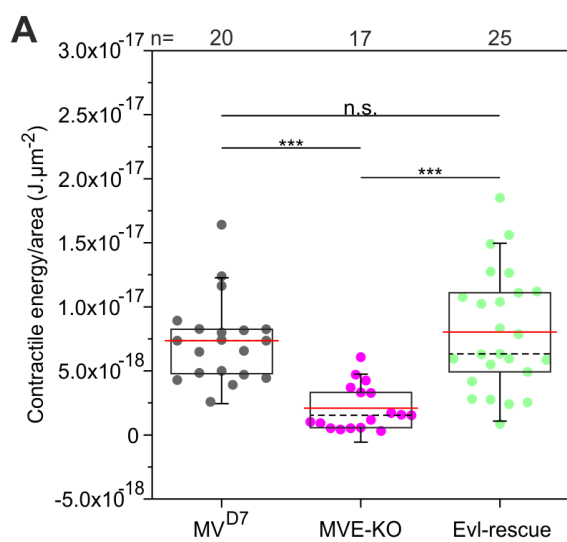MV^{D7} MVE-KO   Evl-rescue

B

MV^{D7} MVE-KO   Evl rescue

500
400
300
200
100
0

Figure 8-figure supplement 1